

Aus dem Institut für Diagnostische und Interventionelle Radiologie  
der Universität Würzburg

Direktor: Professor Dr. med. Thorsten Bley

**Metabolomic Imaging for Human Prostate Cancer Detection  
using MR Spectroscopy at 7T**

INAUGURAL-DISSERTATION

zur Erlangung der Doktorwürde der

Medizinischen Fakultät

der

Julius-Maximilians-Universität Würzburg

vorgelegt von

Romy Langhammer

aus Dresden

Würzburg, Januar 2018



**Referent:** Prof. Dr. Thorsten Bley

**Korreferent:** Prof. Dr. Hubert Kübler

**Dekan:** Prof. Dr. Matthias Frosch

**Tag der mündlichen Prüfung:** 13. Juli 2018

Die Promovendin ist Ärztin.

This project was performed in collaboration with the laboratory of Dr. L. L. Cheng  
(Massachusetts General Hospital, Harvard Medical School, Boston, USA).

Part of this work was presented at the "Joint Annual Meeting of the International Society for  
Magnetic Resonance in Medicine and the European Society for Magnetic Resonance in  
Medicine and Biology" (ISMRM-ESMRMB) in Milano, May 2014  
and at the "95. Deutscher Röntgenkongress" in Hamburg, May 2014.

## Abstract

**BACKGROUND.** Prostate cancer (PCa) remains a major health concern in men of the Western World. However, we still lack effective diagnostic tools a) for an effective screening with both high sensitivity and specificity, b) to guide biopsies and avoid histology sampling errors and c) to predict tumor aggressiveness in order to avoid overtreatment. Therefore, a more reliable, highly cancer-specific and ideally *in vivo* approach is needed. The present study has been designed in order to further develop and test the method of "metabolomic imaging" using magnetic resonance spectroscopy (MRS) at 7T to address those challenges.

**METHODS.** Thirty whole prostates with biopsy-proven PCa were *in vitro* analyzed with a 7T human MR scanner. A voxel grid containing the spectral information was overlaid with the MR image of the middle transverse cross-sectional plane of each case. Subsequent histopathological evaluation of the prostate specimen followed. After the spectral output was processed, all voxels were compared with a metabolomic PCa profile, which had been established within a preliminary study, in order to create a metabolomic map indicating MRS cancer-suspicious regions. Those regions were compared with the histologically identified tumor lesions regarding location.

**RESULTS.** Sixty-one percent of the histological cancer lesions were detected by metabolomic imaging. Among the cases with PCa on the examined slice, 75% were identified as cancerous. None of the tested features significantly differed between detected and undetected cancer lesions. A defined "Malignancy Index" (MI) significantly differentiated between MRS-suspicious lesions corresponding with a histological cancer lesion and benign lesions ( $p = 0.006$ ) with an overall accuracy of 70%. The MI furthermore showed a positive correlation with the Gleason grade ( $p = 0.021$ ).

**CONCLUSION.** A new approach within PCa diagnostics was developed with spectral analysis including the whole measurable metabolome - referred to as "metabolomics" - rather than focusing on single metabolites. The MI facilitates precise tumor detection and may additionally serve as a marker for tumor aggressiveness. Metabolomic imaging might contribute to a highly cancer-specific *in vivo* diagnostic protocol for PCa.

# Table of Contents

<b>List of Abbreviations.....</b>	<b>VI</b>
<b>1. Introduction .....</b>	<b>1</b>
1.1 Prostate cancer - a major health issue .....	1
1.2 Clinically applied prostate cancer diagnostics .....	1
1.2.1 Current state of the art.....	1
1.2.2 Challenges in prostate cancer diagnostics.....	3
1.3 Diagnostic potential of MRS and metabolomic imaging.....	5
1.3.1 MRS using HRMAS: the metabolic face of prostate cancer.....	5
1.3.2 The implementation of MRSI into PCa research .....	6
1.3.3 Metabolomic imaging - results of a preliminary study .....	7
1.4 Objectives of the present study .....	10
1.4.1 Prior investigations.....	10
1.4.2 Objective 1: cancer detection .....	11
1.4.3 Objective 2: prediction of tumor aggressiveness and additional findings .....	12
1.4.4 Objective 3: alternative analysis .....	12
<b>2. Materials and methods.....</b>	<b>13</b>
2.1 Study design and patient population .....	13
2.2 Imaging and data acquisition.....	14
2.2.1 MR Spectroscopy and MR Imaging.....	14
2.2.2 Histopathological evaluation.....	15
2.3 Data processing .....	16
2.3.1 Spectral processing with a MATLAB-based program.....	16
2.3.2 Creation of metabolomic maps .....	18
2.3.3 Definition of MRS cancer lesions .....	20
2.3.4 Processing of the histological data.....	22
2.4 Analysis: metabolomic imaging versus histopathology.....	24
2.4.1 Prior investigation: identification of the corresponding histological middle slides.	24

2.4.2 Alignment of MRS and histological middle slice .....	26
2.4.3 Detection of histological cancer lesions using metabolomic imaging .....	30
2.4.4 Comparison of detected and undetected cancer lesions .....	30
2.5 Alternative analysis .....	32
2.6 Statistical analysis .....	32
<b>3. Results .....</b>	<b>34</b>
3.1 Prior investigation: identification of the corresponding histological middle slides .....	34
3.2 Objective 1 .....	36
3.2.1 Cancer detection using metabolomic imaging .....	36
3.2.2 Differences between detected and undetected cancer lesions .....	38
3.3 Objective 2 .....	38
3.3.1 Estimation of tumor aggressiveness .....	38
3.3.2 Additional findings .....	38
3.4 Objective 3: alternative analysis .....	40
<b>4. Discussion .....</b>	<b>41</b>
4.1 Interpretation of the principal findings .....	41
4.1.1 Original analysis .....	41
4.1.2 Alternative analysis .....	44
4.2 Principal findings in the context of current literature .....	45
4.3 Limitations of the study .....	47
4.3.1 Patient population .....	47
4.3.2 Spectral processing .....	47
4.3.3 Comparison with histopathology .....	48
4.4 Conclusion and outlook .....	49
<b>5. Summary .....</b>	<b>51</b>

<b>Glossary</b> .....	<b>53</b>
<b>List of Figures</b> .....	<b>57</b>
<b>List of Tables</b> .....	<b>58</b>
<b>References</b> .....	<b>59</b>
<b>Appendices</b> .....	<b>70</b>
Construction of the metabolomic PCa profile.....	70
Figures .....	71
Tables .....	74

**Acknowledgements**

**Statement of Authorship**

**Curriculum Vitae**

## List of Abbreviations

<b>3D</b>	three-dimensional
<b>A</b>	surface area
<b>a/b/c</b>	length/width/height
<b>AUC</b>	area under the curve
<b>Avg</b>	Average Voxel Value
<b>(C+C)/C</b>	(choline plus creatine) over citrate
<b>CSR</b>	chemical shift reference
<b>CT</b>	computed tomography
<b>D</b>	distance
<b>d; d1/2</b>	effect size; diameter 1/2
<b>DICOM</b>	Digital Imaging and Communications in Medicine
<b>DRE</b>	digital rectal examination
<b>ERSPC</b>	European Randomized Study of Screening for Prostate Cancer
<b>FOV</b>	field of view
<b>GG</b>	Gleason grade
<b>GS</b>	Gleason score
<b>H&amp;E</b>	hematoxylin-eosin
<b>Hz</b>	hertz
<b>HRMAS <sup>1</sup>H MRS</b>	high resolution magic angle spinning proton magnetic resonance spectroscopy
<b>kHz</b>	kilohertz
<b>L</b>	large
<b>M</b>	medium, median
<b>MGH</b>	Massachusetts General Hospital
<b>MI</b>	Malignancy Index
<b>µm</b>	micrometer
<b>mm</b>	millimeter
<b>MRI</b>	magnetic resonance imaging
<b>MRS</b>	magnetic resonance spectroscopy
<b>MRSI</b>	magnetic resonance spectroscopy imaging

<b>MS</b>	mass spectrometry
<b>N</b>	no
<b>ng/ml</b>	nanogram per milliliter
<b>p, p-value</b>	probability value
<b>PBS-D<sub>2</sub>O</b>	phosphate buffered saline in D <sub>2</sub> O
<b>PC</b>	principal component
<b>PCA</b>	principal components analysis
<b>PCa</b>	prostate cancer
<b>PLCO</b>	Prostate, Lung, Colorectal and Ovarian Cancer Screening Trial
<b>ppm</b>	parts per million
<b>PRESS</b>	point-resolved spectroscopy
<b>PSA</b>	prostate-specific antigen
<b>PSMA-PET</b>	prostate-specific membrane antigen positron emission tomography
<b>pT</b>	pathological tumor stage
<b>ROC</b>	receiver operating characteristic
<b>ROI</b>	region of interest
<b>S</b>	small
<b>SD</b>	standard deviation
<b>T</b>	tesla
<b>T1</b>	tissue relaxation weighting 1
<b>TNM</b>	tumor, lymph nodes, metastasis
<b>TRUS</b>	transrectal ultrasound
<b>V</b>	volume
<b>VS</b>	voxel size
<b>VV</b>	metabolomic voxel value
<b>WD</b>	Weighted Distance
<b>WET</b>	water suppression enhanced through T1 effects
<b>Y</b>	yes
<b>z(ms)/z(tc)</b>	z-coordinate middle slice/tumor center



# **1. Introduction**

## **1.1 Prostate cancer - a major health issue**

Prostate cancer (PCa) continues to be a major health issue, as it is the second most frequently diagnosed cancer in males worldwide<sup>1</sup>. The highest incidence rates are found in the developed countries, such as the USA, with an estimated incidence of 161,360 new cases in 2017<sup>1,2</sup>. Here, 21% of male patients with newly diagnosed cancer suffer from PCa. Based on data collected between 2011 and 2013, every eighth US-American man will develop invasive PCa in his lifetime<sup>2</sup>.

Furthermore, in 2017, an estimated 26,730 men died from PCa in the USA, making PCa the third most frequent cause of cancer death in this country<sup>2</sup>. Nevertheless, PCa is the malignancy with the highest number of survivors in the USA<sup>3</sup>. First, the exceptionally slow and prolonged natural history of localized PCa contributes to this survival rate<sup>4</sup>. Secondly, due to surgical treatment and radiotherapy as well as improved early detection, the 5-year relative survival rate for all stages combined has increased by 32% within the last 25 years and reaches nearly 100% today<sup>3,5</sup>. The 15-year relative survival rate is 95% in the USA<sup>3,6</sup>.

Due to the growth and aging of the global population, the worldwide PCa burden is expected to grow further within the next decades<sup>7</sup>. Therefore, reliable and highly accurate diagnostic tools are needed to select patients for the right individual therapy, in order to improve the overall mortality from PCa while avoiding overtreatment.

## **1.2 Clinically applied prostate cancer diagnostics**

### **1.2.1 Current state of the art**

PCa diagnostics made a great leap forward with the introduction of the prostate-specific antigen (PSA) test in the early 1990s<sup>8</sup>. PSA screening allowed significantly higher detection of the disease, especially at an early, mostly pre-symptomatic stage, and enabled timely therapeutic interventions with the expectation of reducing the mortality<sup>9,10</sup>. Today, 95% of PCa cases are revealed through PSA screening rather than due to symptoms of advanced PCa, such as reduced urinary stream, erectile dysfunction or pain caused by bone metastases<sup>8,11</sup>.

PSA is a glycoprotein primarily produced in the prostate gland. Disruptions of the prostatic architecture, which can be caused by inflammation, trauma, hyperplasia or cancer growth, lead to a release of PSA into general circulation. Consequently, the normally very low serum PSA concentration increases. The monitoring of serum PSA level is a) used as a screening tool for detecting PCa and b) as a tumor marker indicating cancer recurrence after radical prostatectomy<sup>12</sup>.

In PCa screening the PSA test is combined with a digital rectal examination (DRE) since the combination of both reaches a higher sensitivity than each tool alone<sup>13</sup>. However, weighting the benefits of the screening against potential harms due to overdiagnosis and overtreatment of this often slow-growing and non-lethal disease, no American expert organization presently endorses a routine PCa screening for men at average risk<sup>6</sup>. The U.S. Preventive Services Task Force as well as the American Urological Association and the American Cancer Society advocate informed decision making of male patients in cooperation with their health care providers in order to decide in favor of or against a PCa screening<sup>8,12,14</sup>.

Abnormal results in the PSA test or DRE require biopsy sampling of prostatic tissue in order to make a diagnosis. With transrectal ultrasound (TRUS) guidance, core needle biopsies are taken. Here, the number of 12 site samples was proven to achieve the highest detection rate<sup>15</sup>. The specimens are then histopathologically evaluated and cancerous lesions graded according to the Gleason scheme<sup>11,15</sup>. Based on the architectural pattern of the tumor, each lesion is graded with a number from 1 (very well differentiated) to 5 (very poorly differentiated), referred to as "Gleason grade". PCa is characterized by a high morphological heterogeneity with usually more than one histological pattern present within a prostate. Therefore, the most and the second most prevalent Gleason grades form the Gleason score, e.g. Gleason score 3+4=7, which ranges between 2 and 10<sup>11,16</sup>. The Gleason score is proven to be a measure of tumor aggressiveness with high scores indicating high aggressiveness<sup>8,11</sup>.

In patients with diagnosed PCa, computed tomography (CT) or magnetic resonance imaging (MRI), as well as bone scintigraphy or bone X-ray are used for further staging<sup>12</sup>. Clinical findings and histopathological assessment are combined to stage the carcinoma according to the American Joint Committee on Cancer TNM system, with the T-category describing the original tumor, and the N- and M-categories referring to the lymph node involvement and existence of distant metastases, respectively.

Research showed that the pretreatment PSA, Gleason score and clinical tumor stage are independent risk factors for tumor progression, including extra-prostatic extension, seminal vesicle invasion and lymph node involvement<sup>12,17,18</sup>. Therefore, several prognostic nomograms were developed and can be used to estimate tumor progression by applying the parameters mentioned above<sup>19,20</sup>. The results may give some indication about the tumor aggressiveness and hence alleviate therapeutic decisions. The sensitivity of those predictive tools reaches up to 80%<sup>21,22,23,24</sup>.

In cases with no histological PCa at biopsy but consistent high serum PSA levels, repeat biopsy can be necessary within six months<sup>8</sup>. In case of negative biopsies with elevated serum PSA, MRI is increasingly accepted to identify and localize PCa lesions, as well as for guidance of biopsy<sup>25,26,27,28,29</sup>.

Apart from the described diagnostic protocol, a new molecular imaging technique found a wide clinical application: the prostate-specific membrane antigen positron emission tomography (PSMA-PET). PSMA is a cell surface protein with highest expression in PCa cells<sup>30,31</sup>. Research showed promising results regarding primary PCa detection, staging and treatment planning using PSMA-PET<sup>32</sup>. To date, highest detection rates (80-90%) are achieved in metastatic recurrent PCa<sup>33,34</sup>. Furthermore, the degree of expression of PSMA was found to correlate with tumor aggressiveness, hence PSMA might prospectively serve as a prognostic marker<sup>35,36,37,38</sup>.

### **1.2.2 Challenges in prostate cancer diagnostics**

There currently are three major challenges in screening and primary diagnosis of PCa.

The first substantial problem is the interpretation of PSA serum levels. Though PSA screening has revolutionized early detection of PCa, leading to significantly higher incidence and early interventions as mentioned above, the PSA is prostate- but not cancer-specific. Benign prostate conditions, such as inflammation, trauma or hyperplasia might elevate the PSA serum level, leading to false positives<sup>12</sup>. A big European study (n = 182,000) showed, that over 75% of men undergoing biopsy subsequent to an elevated PSA value had a false positive result in the PSA screening<sup>39</sup>. Hence, a considerable number of patients (falsely) receive invasive biopsy sampling, causing severe side effects such as pain, bleeding or infection in about one third of the cases<sup>40</sup>. Additionally, psychological effects, including increased cancer-related worry and sexual dysfunction, occur after a false positive PCa screening<sup>41</sup>. Apart from this,

the benefit of decreasing mortality rates by PSA screening is highly controversial. While the multicenter European Randomized Study of Screening for Prostate Cancer (ERSPC) reported a reduction of the PCa-specific mortality up to 21% after eleven years of screening, but no significant difference in the all-cause-mortality, one of the largest US-American trials, the Prostate, Lung, Colorectal and Ovarian Cancer Screening Trial (PLCO), did not find any effects on the mortality rate<sup>42,43</sup>. Latest reanalyses however revealed a significant benefit in PCa-specific mortality using PSA-screening for the PLCO-population as well<sup>44,45</sup>.

A second serious problem occurs with biopsy sampling. With histopathology currently being the gold standard in PCa diagnosis, a definite diagnosis can only be made by histopathological evaluation<sup>46</sup>. There is a lack of cancer-targeted biopsies, as the standard TRUS has limits to differentiate between malignant and benign prostatic lesions<sup>47,48</sup>. The mostly slow and heterogeneous growth of PCa lesions probably plays a major role in this issue. The consequence is a substantial number of false negatives in histopathological PCa detection, which is reported between 15 and 30% among first biopsy sampling<sup>47,49,50</sup>. In patients with high PSA levels but repeatedly negative biopsies, MRI was proven to increase the detection rate by guided biopsy<sup>27,28,51</sup>. However, Sciarra et al. measured a sensitivity of only 84,6% for MRI-targeted biopsies<sup>52</sup>.

Last, the prediction of tumor aggressiveness and potential progression is still challenging. Localized PCa often is a non life-threatening condition. Using the current diagnostic pathways, an overdiagnosis of those low-risk tumors has been shown, leading to a high rate of overtreatment<sup>53</sup>. This is of relevance since prostatectomy as the main therapeutic intervention causes irreversible side effects such as erectile dysfunction, urinary incontinence and bowel disturbances, with a great impact on the patients' life quality<sup>54,55,56</sup>. Even in patients with low-risk PCa, watchful waiting and active surveillance are rarely applied<sup>57,58</sup>. The challenge is to differentiate between patients with potentially aggressive cancer that need consequent treatment and patients with indolent disease, who might be managed by observation<sup>57</sup>. A more reliable system to predict tumor aggressiveness and progression is needed. A first step was done with the introduction of empirical nomograms, applying PSA value, Gleason score and clinical tumor stage for the estimation of tumor progression as mentioned above. However, invasive biopsy sampling is needed for this procedure and the sensitivity and specificity still need to be improved. Apart from this, PSMA is a promising new marker for tumor aggressiveness, with further research to be performed.

In summary, new cancer-specific diagnostic tools are required in order to decrease the number of false positives in primary PCa diagnosis. Radiological techniques such as MRI that indicate suspicious prostatic regions for selective biopsy sampling need to be improved. Finally, reliable non-invasive imaging tools for the prediction of tumor aggressiveness and progression would contribute to a more reasonable therapy decision, avoiding highly aggressive procedures in patients with low-risk PCa and strengthening the patients' and doctors' trust in tumor observation (active surveillance).

### **1.3 Diagnostic potential of MRS and metabolomic imaging**

#### **1.3.1 MRS using HRMAS: the metabolic face of prostate cancer**

Many of those challenges among PCa diagnostics can potentially be addressed by magnetic resonance spectroscopy (MRS) in general and magnetic resonance spectroscopy imaging (MRSI) in particular.

Compared to current imaging techniques such as MRI, CT or ultrasound, MRS investigates the biochemical background of tumorous tissue<sup>59</sup>. Using MRS, alterations of metabolites in cancer development can be detected, making MRS a highly cancer-specific method<sup>60</sup>. Furthermore, compared to mass spectrometry (MS), MRS has the significant advantage of a possible *in vivo* translation, as the histological structure of tissue samples is not altered during analysis<sup>61</sup>.

Cancer cells are highly proliferative and show specific alterations in metabolic pathways that can be detected using MRS<sup>59,62</sup>. In PCa research, the most commonly applied metabolite markers are citrate and choline. PCa cells are characterized by a lower citrate and higher choline level compared to benign prostatic tissue<sup>63,64,65</sup>. Citrate in particular plays a central role in the development of prostate malignancy. Due to its function in sperm production, healthy prostatic tissue has the ability to produce, accumulate and secrete high amounts of citrate, leading to 30-50 fold higher intracellular citrate concentrations compared to other parts of the human body. Cancer cells lose their enzymatic capability to accumulate and secrete citrate due to loss of differentiation. Instead, citrate is consumed for energy metabolism in order to enable the increased turnover of cancer cells, resulting in low citrate levels. This transformation in the use of the citrate seems to be essential for the development of PCa<sup>66,67,68</sup>. Moreover, the increase of choline among PCa cells reflects the elevated cell

proliferation rate of the malignant tissue as the cell membrane synthesis is stimulated<sup>69,70,71</sup>. Other examples of metabolic markers for PCa are creatine, spermine, myo-inositol and amino acids such as alanine, lysine, sarcosine and taurine<sup>63,72,73,74</sup>.

When the first steps in characterizing metabolic markers of PCa using MRS were made, a major problem was faced: classical MRS has been developed for the analysis of aqueous solutions such as extracts and lysed cell solutions. Among solid samples, however, molecules experience anisotropic effects, causing spectral line broadening and therefore low resolution, hindering the distinction of individual metabolites. In consequence, MRS of solid tissue was of limited use, whereas conventional MRS using aqueous solutions did not allow subsequent histopathological evaluation<sup>72,75,76</sup>. A great improvement was the introduction of high resolution magic angle spinning proton magnetic resonance spectroscopy (HRMAS <sup>1</sup>H MRS) in 1996, which revolutionized the *ex vivo* research of PCa. By spinning the solid sample at a "magic angle" of 54.7° with respect to the magnetic field, anisotropic interactions were averaged to isotropic levels. Consequently, line-narrowing and a significant increase of resolution were achieved, allowing the identification and quantification of individual metabolites among solid samples without sacrificing the tissue architecture<sup>75,77,78,79,80</sup>. In summary, HRMAS <sup>1</sup>H MRS enables a detailed biochemical analysis of solid specimens while preserving the tissue for subsequent histopathological evaluation. Therefore, this technique was intensively applied in cancer research, including PCa<sup>63,81,82,83,84</sup>.

### **1.3.2 The implementation of MRSI into PCa research**

The introduction of HRMAS <sup>1</sup>H MRS into PCa research paved the way for the implementation of magnetic resonance spectroscopy imaging (MRSI). MRSI combines the metabolic information of a sample provided by MRS with the illustration of the same sample obtained by conventional MRI. More precisely, a region of interest is defined among the anatomical image and broken into a voxel grid. Subsequently, selected spectroscopic data is acquired for each voxel and overlaid with the anatomical image. MRS data thus provides a metabolic map that can be correlated with the information obtained by MRI, such as tumor size and volume<sup>59,72</sup>.

After the first successful application of the MRSI technique within brain tumor research, the method was implemented to PCa studies<sup>61,85</sup>. It has been shown that the combination of MRS and MRI significantly improved the cancer detection rate compared to each method alone<sup>86</sup>.

In particular the use of HRMAS  $^1\text{H}$  MRS significantly increased the sensitivity for PCa detection<sup>84,87</sup>.

Initially, single metabolites or metabolite ratios were analyzed in order to reveal the molecular changes in cell metabolism of PCa cells<sup>59,88,89,90</sup>. In particular the ratio of (choline+creatine)/citrate, shortly (C+C)/C, seems to have a strong potential to improve accuracy in PCa detection<sup>91,92,93</sup>. Here, the classification of Kurhanewicz et al. was primarily applied, with ratio values of lower than 0.75 characterizing normal prostatic tissue, whereas values between 0.75 and 0.86 were considered as suspicious and ratios above 0.86 as definitively malignant<sup>94,95</sup>. With the ratio (C+C)/C and a cut-off value of 0.75, a pooled weighted sensitivity of 82% in detecting PCa was achieved<sup>86,95,96,97,98,99</sup>. Moreover, this ratio demonstrated its potential to predict tumor aggressiveness by correlating with the tumor's Gleason score and identifying extracapsular expansion and invasion in surrounding tissue<sup>99,100</sup>. However, it was proven to be poor at detecting low-grade tumors, as the sensitivity of the ratio improved with increasing Gleason scores. Malignant lesions with a Gleason score of 3+3 were detected with a sensitivity of 44%, whereas for Gleason scores of 4+3 and higher, detection rates of over 85% were achieved<sup>100</sup>. In summary, the technique of MRSI in association with the (C+C)/C ratio achieved promising initial results in PCa detection and prediction of tumor aggressiveness.

### **1.3.3 Metabolomic imaging - results of a preliminary study**

As described above, the majority of metabolic research on PCa has focused on a small group of metabolites that have long been known to correlate with prostatic malignancy. However, efforts at profiling the entire measured metabolome rather than focusing on individual metabolites have been increased<sup>101</sup>. Thus, a more complete depiction of the metabolic alterations among the development of cancer cells could be achieved<sup>102,103,104,105</sup>. The concept of investigating the whole metabolome was named "metabolomics" and is derived from the field of genomics and proteomics, where studies of isolated genes and proteins evolved to research of the whole measurable genome and proteome as well as their correlations under physiological and pathological conditions<sup>106</sup>.

In an in-lab pilot study in 2005, 199 *ex vivo* samples of 82 PCa patients were analyzed using HRMAS  $^1\text{H}$  MRS at 14T, with subsequent histopathological evaluation. It was successfully demonstrated that metabolomic profiles obtained from those samples were stronger in

identifying cancer regions than individual metabolites. An overall accuracy for differentiating between histologically benign and malignant lesions of 98.2% was achieved. Furthermore, positive correlations between the metabolomic outcome with the patients' serum PSA value before prostatectomy, tumor pathological stage and perineural invasion were revealed<sup>84</sup>.

This pilot study unveiled the potential of metabolomic techniques in detection of PCa and in prediction of tumor aggressiveness. Recognizing this diagnostic potential of metabolomic profiles among PCa research, another study (further referred to as "preliminary study") was performed to improve the capacity of locating and assessing malignancy in prostates by combining metabolomic profiles with the technique of MRSI (as MRSI has the perspective of an *in vivo* approach)<sup>104</sup>.

First, a metabolomic PCa profile that included the specific alterations of prostate cancer cells in 36 metabolic regions was developed (for a more detailed description, see Appendix, p. 70). In order to compare the MR spectrum of a prostatic sample with this cancer profile, the intensities of the 36 metabolite regions were combined with the "overall loading factors" of each region. These overall loading factors measured how the metabolite regions were altered in PCa. The more a region contributed to the cancer profile, the higher the overall loading factor. The result was a metabolomic profile value that quantified to what extent the MR spectrum correlated with the metabolomic profile, thus reflecting the possibility for malignancy.

Due to the absence of a metabolomic profile that was specific for measurements of prostatic tissues at magnetic field strengths of 7T, the profile was obtained from previous analyses with the 14T HRMAS <sup>1</sup>H MR spectrometer, having been conducted during the pilot study mentioned above<sup>84</sup>. A phantom study with the intention to test the validity of this metabolomic PCa profile obtained at 14T successfully proved the applicability of 7T whole prostate spectral data<sup>104</sup>.

The metabolomic PCa profile was then tested with 15 malignant and 27 benign prostatic samples of 13 patients. It showed an overall accuracy of 93% for detection of malignancy. Furthermore, the median (M) as well as standard deviation (SD) of the 42 samples were calculated. Notably the metabolomic voxel values of all histologically benign samples fell below the empirical threshold of median plus one standard deviation ( $M+SD$ ) (Figure 19, appendix p. 71) with metabolomic voxel values above this level indicating PCa.



Following the implementation of a PCa-specific metabolomic profile, an *ex vivo* analysis of five whole prostates (each with Gleason score 7; pathological tumor stage (pT): four lesions of pT2, one of pT3) after prostatectomy (from patients with biopsy-proven PCa) was conducted. MRSI of the middle transverse cross-sectional plane was performed with a 7T human whole-body MR scanner. Using the metabolomic PCa profile, MRS cancer-suspicious regions (with metabolomic voxel values above the threshold ( $M+SD$ )) were identified and mapped on the MR image and subsequently histopathologically evaluated.

Thirteen MRS-suspicious regions were detected and five of those profile-elevated regions corresponded with one of the five histologically verified PCa lesions. The remaining eight MRS-suspicious regions were considered as histologically benign (however with elevated profile values). To compare the MRS-suspicious regions among different cross-sectional planes from different prostate samples, a "Malignancy Index" (MI) was defined, which sums up the total elevation of the metabolomic voxel values of this region. The MI demonstrated its potential to significantly differentiate between malignant and benign MRS-suspicious regions with an overall accuracy of 93% for all five cancer lesions and 97% for the four pT2 lesions (Figure 20, appendix p. 71). Moreover, among the four pT2 tumors, the MI correlated with the histologically determined tumor size. This effect may be a result of a MI being strongly influenced by the high number of pT2 tumor samples.

In addition, the "Weighted Distance" (WD) index was defined as the range between the center of the histological cancer lesion to the center of the corresponding MRS suspicious lesion, normalized by the number of voxels included. The WD was then compared with the average voxel intensities of the MRS-suspicious region. As expected, an inverse linear correlation was found among the pT2 tumor lesions, suggesting higher MRS metabolomic profile values close to the center of the corresponding histological cancer lesion (Figure 21, appendix p. 72).

As the ratio  $(C+C)/C$  had been widely examined in the field of metabolic PCa research, prostate samples were then analyzed using this ratio rather than the metabolomic profile (including 36 metabolite regions). None of the  $(C+C)/C$  maps was able to detect a cancer lesion with statistical significance. This was probably due to the limited sample size. However, these findings underline the potential of metabolomic profiles in diagnosing PCa, in contrast to metabolic ratios considering only a few individual metabolites.

Our preliminary study thus revealed a promising value of metabolomic profiles in PCa diagnostics. Especially the MI served as a solid tool to identify MRS-suspicious regions of

malignant origin. Nevertheless, those findings were preliminary with respect to the small sample size. Moreover, the whole spectral processing was carried out manually using the software NUTS (Acorn NMR NUTS, Version 20071214, Livermore, CA, USA, 2007). This process proved to be extremely time-consuming: the processing of one cross-sectional plane with 256 voxels demanded more than a man-month<sup>107</sup>.

With the preliminary study, a new method with regards to MRSI was established and the PCa-specific metabolomic profile was tested. This research was of high interest to be extended to a larger study with a higher number of samples. For a decent duration of the technique, a partial automation of the procedure was strongly required.

#### **1.4 Objectives of the present study**

This study is designed in order to further test the metabolomic PCa profile regarding cancer detection and prediction of tumor aggressiveness. In order to evaluate the profile's strength, the metabolomic imaging output will be compared with the histopathological findings, as histopathology is currently regarded as the gold standard in PCa assessment<sup>46</sup>.

Compared to the preliminary study described above, the sample size will be increased to 30 whole prostates. Furthermore, an in-house analyzing tool will be applied to automate parts of the spectral processing and to reduce the analysis time to a manageable level<sup>107</sup>.

##### **1.4.1 Prior investigations**

For a comparison between metabolomic maps and histological findings, two conditions need to be addressed. First, the prostate plane chosen for analysis - in this study the middle transversal slice - has to be clearly identified within the MRSI slices and histological slides. Second, a precise alignment of corresponding MRSI slice and histological slide is needed.

In contrast to the MRSI data which include the scan of the center plane, the histological slides provide no precise visual identification of the middle slice due to specimen preparation. To address this issue, a prior objective of the study is to develop a technique that identifies the histological slide of the most central location within the prostate. It is intended to graph an equivalent of the prostate plane surface values against the corresponding slide numbers and then compare the graph with the typical prostate shape.

Furthermore, it has to be approved that the MRI/MRS scan is acquired precisely from the middle cross-sectional plane of each specimen without a relevant temporary deformation and compression of the prostates' base and apex during the scan due to gravity. This would cause an increase in surface of the bottom slices and a shifted middle slice. Thus it is planned to graph the surfaces of the MRSI slices against the slice numbers and to compare this graph with the typical prostate shape as well as the graph calculated for the surfaces of the histological slides, in order to rule out a relevant specimen deformation during the scan.

A second prior objective is to develop a method for a precise alignment of MRSI and histological slices. The directions of the histological slides with respect to the anatomical position of the prostate are marked by the pathologist. In contrast, among the MRSI data there are small variations regarding the orientation of the prostates during the MR scanning which need to be compensated. Thus, a method to precisely recognize the MR slice boundaries right/left and anterior/posterior has to be established in order to perform a correct alignment of MRSI and histological middle slice.

#### **1.4.2 Objective 1: cancer detection**

The primary objective of the present study is to test the metabolomic imaging technique using a metabolomic PCa profile regarding detection of cancer lesions within 30 prostate samples. It will be investigated, whether the variables Malignancy Index (MI) and Average Voxel Value (Avg) might differentiate MRS-suspicious regions detecting a histological cancer lesion from those regions with elevated profile values but benign histology. The hypothesis is that MI and Avg may successfully detect MRS-suspicious regions that identify a histologically proven cancer lesion.

In case that histologically proven cancer lesions are not detected by metabolomic imaging, it will be analyzed, whether characteristics such as tumor volume, Gleason grade, pathological tumor stage and distance from the tumor center to the spectrally analyzed prostate plane differ from the detected tumors. It is hypothesized, that undetected cancer lesions may be of lower volume as well as lower Gleason grade and pathological T-stage compared to detected cancer lesions, and that the tumor centers are located more distant from the spectrally analyzed prostate plane.

### **1.4.3 Objective 2: prediction of tumor aggressiveness and additional findings**

As a secondary objective it will be tested if tumor aggressiveness can be predicted by metabolomic imaging. MRSI outcome (MI, Avg) will be correlated with markers of tumor aggressiveness (Gleason grade and T-stage). A positive correlation between MI/Avg and Gleason grade/pathological tumor stage is expected.

It is furthermore hypothesized that tumors of higher volume and with centers being located approximate to the MRS-suspicious region may induce higher metabolomic profile values and therefore higher MIs and Avgs.

### **1.4.4 Objective 3: alternative analysis**

The definition of which voxels are considered as PCa-suspicious (metabolomic profile value above the threshold ( $M+SD$ )) is of empirical character and was developed within the preliminary study. It had been shown that all benign voxel values fell below the threshold of ( $M+SD$ ) (Figure 22, appendix p. 72). At the same time, values of malignant voxels were found below this threshold as well. Consequently, malignant regions may be missed using this threshold. To address this issue, the threshold for metabolomic voxel profile values to be considered as suspicious will be reduced to ( $M+0.75SD$ ) in an alternative analysis. It is expected that more cancer lesions may be detected with this new threshold. However, the number of false positive MRS-suspicious regions (as they correspond with a benign histology) may increase, resulting in a lower power of MI and Avg.

## 2. Materials and methods

### 2.1 Study design and patient population

The present study is designed as an *ex vivo* study and was approved by the Institutional Review Board at Massachusetts General Hospital (MGH) in Boston, USA.

Thirty whole prostates were collected from male patients with biopsy-proven cancer who underwent radical prostatectomy at the Department of Urology at MGH between 2007 and 2009. Mean patient age at the time of surgical intervention was 58.4 years, with a standard deviation of 5.8 years. The glands weighed 45.1g on average, with a standard deviation of 13.0g. The Gleason score (GS) ranged from GS6 (12 samples, 40%) to GS8 (4 samples, 13%) and 14 of the samples (47%) had GS7. In terms of TNM classification, most of the patients had a pathological tumor stage (pT) of 2 (pT2a: 6 specimens, 20%; pT2b: 5 specimens, 17%; pT2c: 16 specimens, 53%), whereas there were only few samples with pT1 (pT1c: 1 specimen, 3%) or pT3 (pT3a and pT3b: 1 specimen, 3% each) and no cases of pT4. Lymph node spread and metastases were negative or not determined. Details for the individual cases are presented in Table 1.

Case #	Age at surgery	Weight of gland [g]	Prostate dimensions	Gleason score	TNM stage
1	55	41	4.6 x 4.2 x 4.0 cm	3+4=7	pT2a N0 M0
2	61	46	5.0 x 4.0 x 3.5 cm	3+4=7	pT2b Nx Mx
3	62	41	4.5 x 4.0 x 3.5 cm	3+4=7	pT3b Nx Mx
4	57	82.9	5.5 x 5.5 x 4.5 cm	3+3=6	pT2a Nx Mx
5	60	75	6.0 x 5.5 x 5.0 cm	3+3=6	pT2a N0 Mx
6	62	51	4.5 x 4.2 x 3.9 cm	3+4=7	pT2c N0 Mx
7	57	40	4.5 x 4.0 x 3.5 cm	3+3=6	pT2c N0 Mx
8	66	53	5.5 x 4.5 x 4.5 cm	4+4=8	pT2a N0 Mx
9	61	33.9	4.5 x 4.5 x 4.5 cm	3+4=7	pT2c Nx Mx
10	56	40	4.5 x 4.3 x 3.5 cm	3+3=6	pT2c Nx Mx
11	60	40.3	4.8 x 4.3 x 4.0 cm	3+3=6	pT1c Nx M0
12	47	19.1	3.8 x 3.8 x 3.2 cm	3+4=7	pT2c Nx Mx
13	56	48	5.5 x 5.5 x 4.5 cm	3+4=7	pT2c Nx Mx
14	64	36	5.5 x 5.1 x 4.5 cm	3+3=6	pT2a Nx Mx
15	52	40	4.8 x 4.0 x 3.6 cm	3+4=7	pT2c Nx Mx
16	52	53	5.8 x 4.5 x 4.2 cm	3+3=6	pT2c Nx Mx
17	56	46.6	5.2 x 4.5 x 4.2 cm	3+3=6	pT2c Nx Mx
18	56	31.3	4.5 x 4.2 x 4.0 cm	4+4=8	pT2b Nx Mx
19	60	42.5	5.5 x 4.5 x 4.5 cm	3+4=7	pT2c Nx Mx
20	60	57.8	5.5 x 5.2 x 4.5 cm	4+4=8	pT3a Nx Mx

21	53	38.5	4.5 x 4.0 x 3.7 cm	3+4=7	pT2b Nx Mx
22	71	46.4	4.7 x 4.6 x 4.5 cm	4+4=8	pT2b Nx Mx
23	64	46.3	4.7 x 4.5 x 4.0 cm	3+4=7	pT2c Nx Mx
24	62	67.9	6.7 x 5.5 x 5.2 cm	3+4=7	pT2c Nx Mx
25	59	42.6	4.3 x 4.2 x 3.8 cm	3+3=6	pT2c N0 Mx
26	49	38.7	4.6 x 4.0 x 4.0 cm	3+4=7	pT2a Nx Mx
27	48	29	3.5 x 3.0 x 3.0 cm	3+3=6	pT2c N0 M0
28	53	37.6	5.0 x 3.5 x 1.0 cm	3+3=6	pT2c N0 Mx
29	69	37.9	5.0 x 5.0 x 3.0 cm	3+3=6	pT2b Nx Mx
30	63	51	5.4 x 4.5 x 3.8 cm	3+4=7	pT2c Nx Mx

**Table 1 Patient population.** Age at surgery, weight, prostate size as well as Gleason score and TNM stage after prostatectomy.

## 2.2 Imaging and data acquisition

### 2.2.1 MR Spectroscopy and MR Imaging

Following prostatectomy, the whole prostates were transferred to the Radio-Pathology Laboratory in an icebox. MRI and MRS were conducted the same day at room temperature, using a 7T whole-body human MR scanner (Siemens, Erlangen, Germany).

The prostate specimens were tied into a sample holder to prevent any movement and embedded in phosphate buffered saline in D<sub>2</sub>O (PBS-D<sub>2</sub>O), in order to compensate the magnetic susceptibility at the prostates' border regions. A circular 7cm diameter surface coil was placed axially around the middle of the prostate and served as transmitter and receiver. Regarding the sectional plane, transverse slices were acquired, referring to the prostates' physiological position in the human body.

T2-weighted MR images were obtained (29 slices, 1mm thickness) with a turbo spin-echo sequence and a field of view (FOV) - depending on the gland size - of between 40mm x 40mm and 56mm x 56mm. Two-dimensional multivoxel proton MRS was acquired for three different levels of prostate slices: a middle slice approximately at coil level and two more slices 6mm above and below. For this acquisition, echo time/repetition time of 30/1700 point-resolved spectroscopy (PRESS) with WET (water suppression enhanced through T1 effects) was applied, using a spectral width of 4.0kHz and a water suppression bandwidth of 130Hz. Subsequently, the MRS FOV, which had the same size as the reference MRI FOV, was partitioned into 16 x 16 phase-encoding steps, leading to a total of 256 voxels (Figure 1). As the FOVs differed from sample to sample according to distinct prostate gland sizes, the voxel

measures of different prostate specimens also varied slightly. Each MR scan required a scanning time of approximately 23 minutes.

Regarding the following processing and analysis of the MR data, only the middle cross-sectional planes were part of the present study.

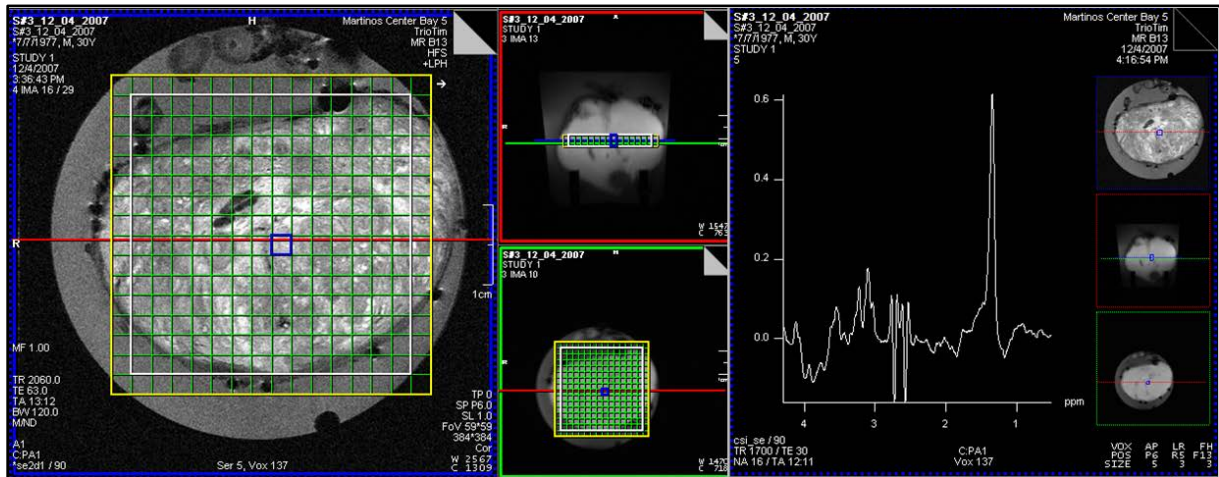


**Figure 1** Screenshot of 7T scan. Left: MR Image and MR Spectroscopy were overlaid during the scan. The MRS FOV was then partitioned into a 16 x 16 voxel grid. One center voxel is picked and highlighted with a blue frame. **Top center:** prostate sample, being fixed in the sample holder, **bottom center:** currently scanned middle transversal slice. **Right:** prostatic spectrum (MRS) of the blue framed voxel.

## 2.2.2 Histopathological evaluation

As the MRS technology produces highly-resolved spectra without damaging the histological architecture of the tissue<sup>84</sup>, a conventional histopathological evaluation of all samples was performed by the Department of Pathology at MGH.

Following MRI/MRS, the whole prostates were fixed in 10% formalin, embedded in paraffin, sliced transversely in 5mm intervals with a thickness of 5 $\mu$ m and stained with hematoxylin-eosin (H&E) according to MGH standard procedure protocols. Depending on the glands' size, serial block sections of four to ten slides were obtained.

Subsequently, a pathologist identified the histological tumor regions with corresponding Gleason grades (GG) (according to the international consensus on Gleason grading of 2005<sup>16</sup>) and marked those lesions by circling them on the glass slide.

## 2.3 Data processing

### 2.3.1 Spectral processing with a MATLAB-based program

For import, processing and analysis of the spectral data, an in-house MATLAB-based analyzing tool, developed by Yannick Berker in 2010, was used. In contrast to other data processing software such as AcornNMR-NUTS (which was the processing tool of the preliminary study<sup>104</sup>), this MATLAB program automates multiple parts of the procedure, thereby expediting the spectral processing<sup>107</sup>.

During scanning, spectral data were saved as Siemens .rda files, whereas the MR images were pooled in DICOM files. While importing a .rda file, the MATLAB program automatically performed a Fourier transformation, transforming the spectral data from the time domain into the frequency (also called "Fourier") domain. In a next step, the program overlaid the MRS voxel grid and the anatomical reference MR image, including equal positioning and alignment.

A region of interest (ROI) was then manually defined among the 256 voxels, in order to limit the processing steps to the prostatic tissue and to reduce the preprocessing and analysis of voxels without useful metabolomic information. The ROI boundaries were drawn at the borderline between prostate gland and fluid in the MR image (Figure 2). Finally, the spectra from voxels containing both tissue and surrounding fluid were individually evaluated and classified as prostatic spectra (and included into the ROI), or as spectra of the surrounding fluid (and subsequently removed from the ROI).

In a next step, a centrally located voxel of the ROI was randomly chosen and a manual correction in phase and baseline was performed. Using the global phase of this voxel, the program initiated a quick preprocessing of all voxels within the ROI, in order to simplify and accelerate the process of by-hand corrections (Figure 3).



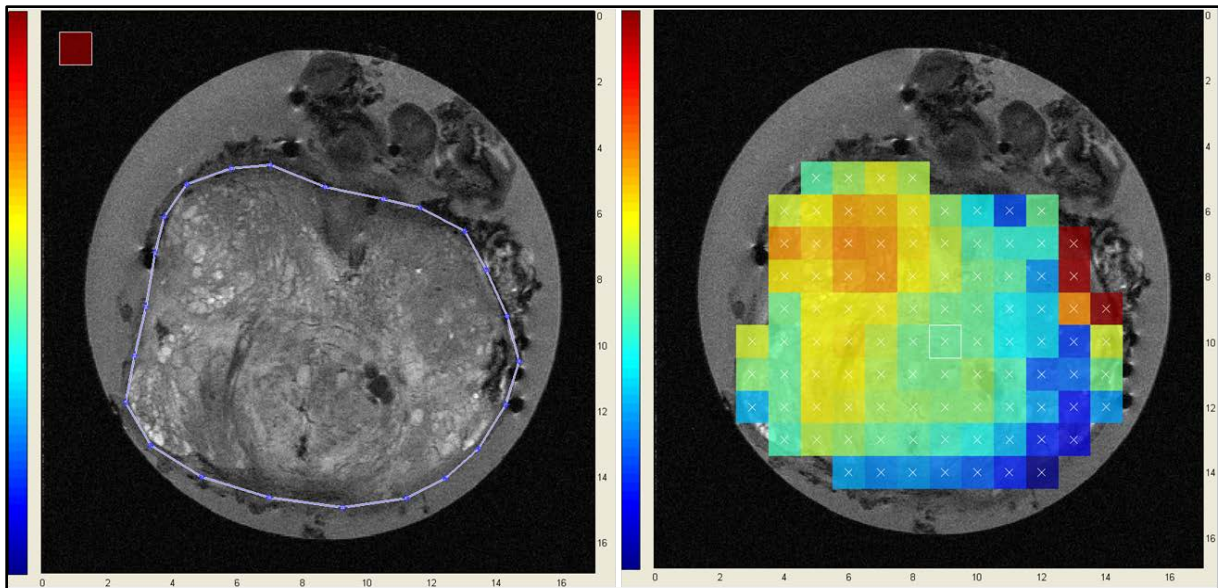


**Figure 2 Definition of the MRS region of interest in MATLAB.** Using the MR Image, a region of interest for the MRS voxel grid was manually drawn (**left**), in order to exclude non-prostatic voxels. **Right:** display of the updated MRS voxel grid. The colors of the voxels shown here do not have a diagnostic value at this stage.

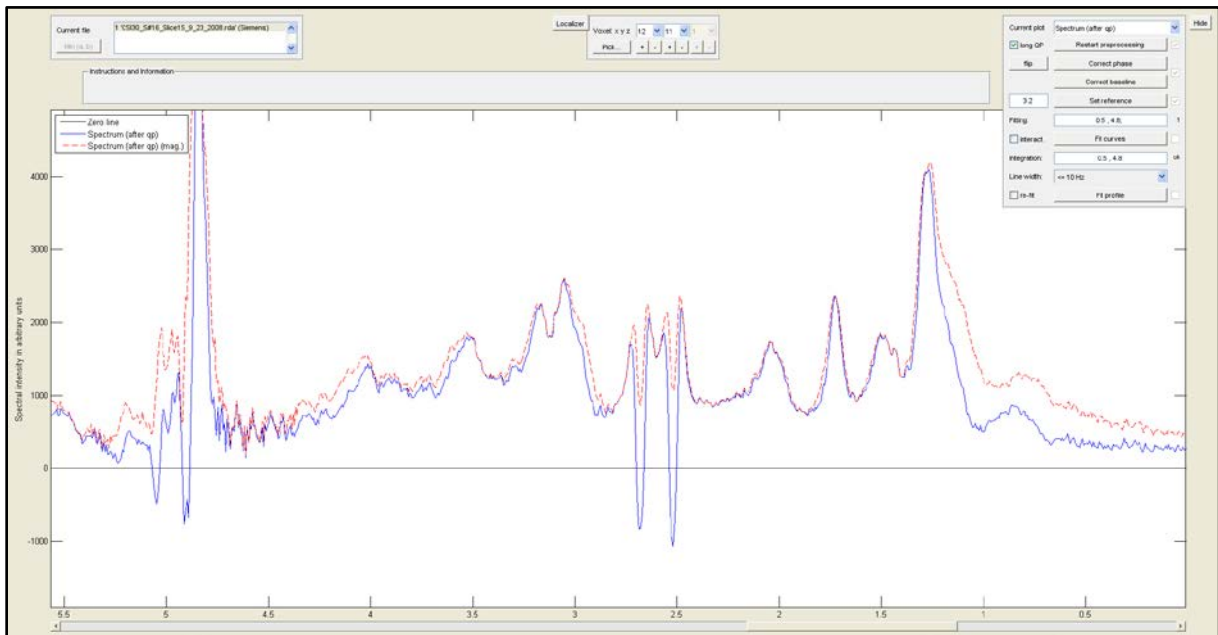


**Figure 3 Voxel spectrum after automatic preprocessing.** By applying automated preprocessing, the MATLAB program already provided an improved phase of the spectrum. However, manual phase correction had to be performed and the baseline needed to be corrected.

The spectral region of interest spanned from 0.5ppm to 4.5ppm<sup>104</sup>. However, in the region between 4.0ppm and 4.5ppm, the peaks of most cases were observed to be highly distorted by the large and broad water peak at around 5.0ppm - even after water suppression during the scan. Therefore, only the region between 0.5ppm to 4.0ppm was processed and analyzed (Figure 4).

Within the established spectral region of interest, the correction in phase and baseline for each voxel was performed manually. First and zero order phase correction, mostly using the lipid peak at 1.3ppm as the zero order reference point, was used to keep the peaks as narrow and

symmetric as possible. With the baseline correction, the correct orientation of the spectrum with respect to the horizontal zero line was achieved. Subsequently, a chemical shift reference (CSR) was set by adjusting the narrow choline peak to be located exactly at 3.2ppm. Hence, the whole spectrum was shifted horizontally, matching the x-axis frequency values in ppm to the commonly known positions of prostatic metabolites. As a control, it was ensured that the lipid peak was located at 1.3ppm, as well as the citrate peak between 2.5ppm and 2.7ppm (Figure 4).

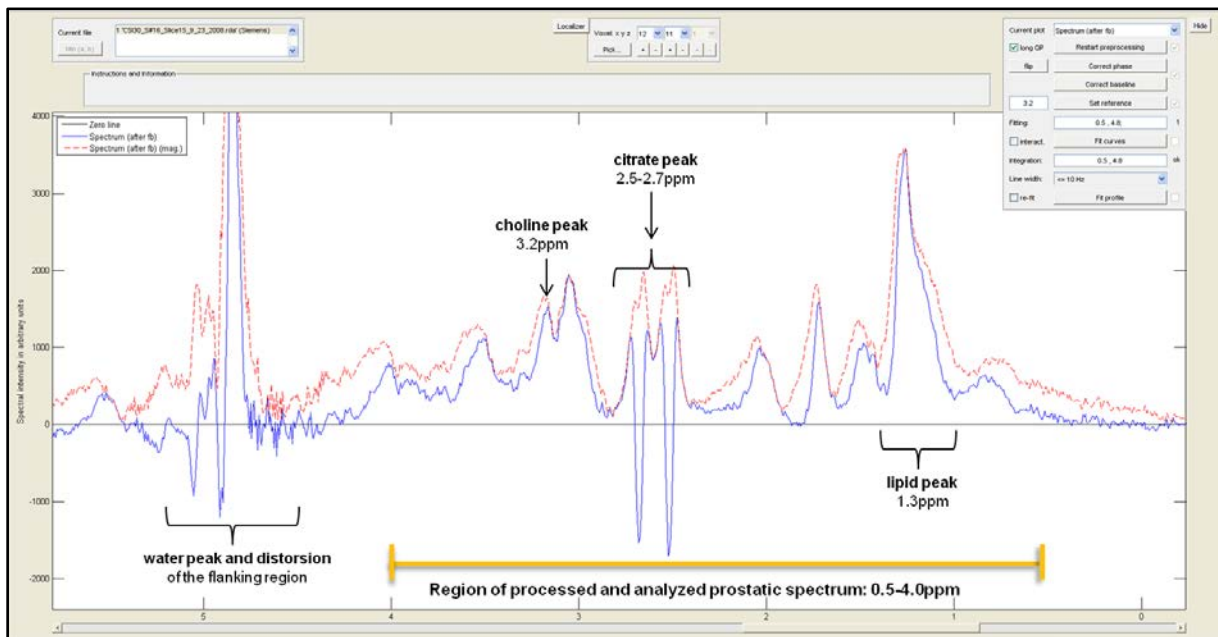


**Figure 4 Voxel spectrum after manual correction.** After phase and baseline correction, the peaks had a symmetric phase and were located on the baseline. The choline peak was located at 3.2ppm, the citrate peak at 2.5-2.7ppm, whereas the broad lipid peak was located around 1.3ppm. Note the incompletely suppressed water peak at 5ppm, which effected a high distortion of the curve between 4.0 and 4.5ppm. In consequence, only the region between 0.5 and 4.0ppm was included into spectral analyses.

In summary, the spectral data of prostatic origin were identified at that point and the partly automated, partly manual processing was completed. Compared to the preliminary study, the time frame for the spectral processing was successfully reduced to 6-8 hours of manual corrections per case, depending on the size of the sample slice as well as the experience of the operator.

### 2.3.2 Creation of metabolomic maps

As the spectral data was fully processed and thus prepared for analysis, a metabolomic map for each prostate's center cross-sectional plane was created. In a "Profile Fitting" process, the metabolomic PCa profile obtained in the preliminary study was applied to the voxel grids in order to analyze, to what extent each voxel was cancer-suspicious. The output of the Profile

Fitting was a) a visual metabolomic map of each analyzed prostate slice, indicating regions with a cancer-suspicious metabolite spectrum; and b) the numeric export of each voxel's metabolomic value into an Excel file (the higher the value, the more cancer-suspicious the voxel). In contrast to the preliminary study, the whole Profile Fitting was an automated process performed by the MATLAB program. It took eight hours per case and was performed as an overnight task.

The first step of the Profile Fitting was the measurement of all positive peak intensities per voxel. Then, the intensities of all 36 metabolite regions that were included in the metabolomic PCa profile were multiplied with their individual overall loading factors and then summed up. The result was the voxel's metabolomic value, indicating how suspicious the spectrum was to for malignancy. For a full list of the overall loading factors see Table 4 (Appendix, p. 74).

In order to average out noisy influences, data smoothing was conducted as a part of the automated Profile Fitting. Therefore, each voxel value was replaced by a weighted sum of the values of the surrounding voxels and its own by using a two-dimensional convolution matrix, in order to obtain a smoothed voxel value. This value consisted of one quarter of its own normalized value, one-eighth of each direct neighbor's, and one-sixteenth of each diagonal neighbor's value. For edge voxels, the calculation was slightly different due to the lack of surrounding voxels on each side (Table 2).

1	2	1
2	4	2
1	2	1

2	4	2
1	2	1

**Table 2 Convolution matrix for smoothing of voxel cancer values in order to reduce noise effects.** Shown are the weights of the values, contributing to the smoothed value of the center voxel, marked in dark gray. Directly neighbored voxels have a higher impact than the diagonal neighbors. **Left:** matrix for inner voxels, surrounded by eight adjacent voxels. To gain the smoothed value for this voxel, the values of the voxels are multiplied by the weights and summed up, then divided by 16. **Right:** For voxels on the edge of the prostate slice, being surrounded by less than eight other voxels, the calculation is the same, except from the divisor, which would be 12 in this case. Thus, the different values have a bigger impact on the smoothed voxel value, than they would have in the slice center.

Finally, the voxels of the whole grid were mapped to a color scale, with cancer-suspicious profile values colored towards red and unsuspecting voxels towards blue (Figure 5).

The smoothed metabolomic voxel values were then exported into an Excel workbook, ready for further quantitative analysis.

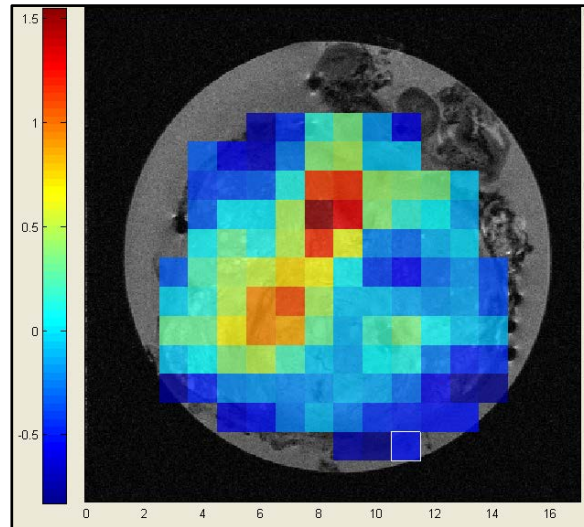


**Figure 5 Metabolomic cancer map after Profile Fitting.** The voxels of this prostatic middle slide are colored due to their smoothed voxel values, with higher values (being more cancer-suspicious) mapped in red tones and low values (being less suspicious) colored in greens and blues. There are two central regions with high potential for malignancy.

### 2.3.3 Definition of MRS cancer lesions

While the visual metabolomic map created by MATLAB for each prostate's middle transverse slice served as an orientation, a manual quantitative analysis of the metabolomic voxel values was inevitable for a reliable definition of MRS-suspicious regions.

A threshold for consideration as cancer-suspicious had been defined in the preliminary study. Voxel values higher than  $(M+SD)$ , with mean and standard deviation calculated for all smoothed voxel values of a prostate plane, proved to be a significant indication of cancer<sup>104</sup>.

In the created Excel file, all metabolomic voxel values were listed in a grid with respect to voxel location among the prostate slide. A function allowed the definition of a threshold, which was determined as  $(M+SD)$  in this case. Consequently, voxels with a value above the threshold (being considered as suspicious) were listed as "1", while the rest was marked with a "0", (Figure 6A). Thus, a quick analysis of the voxel values was possible.

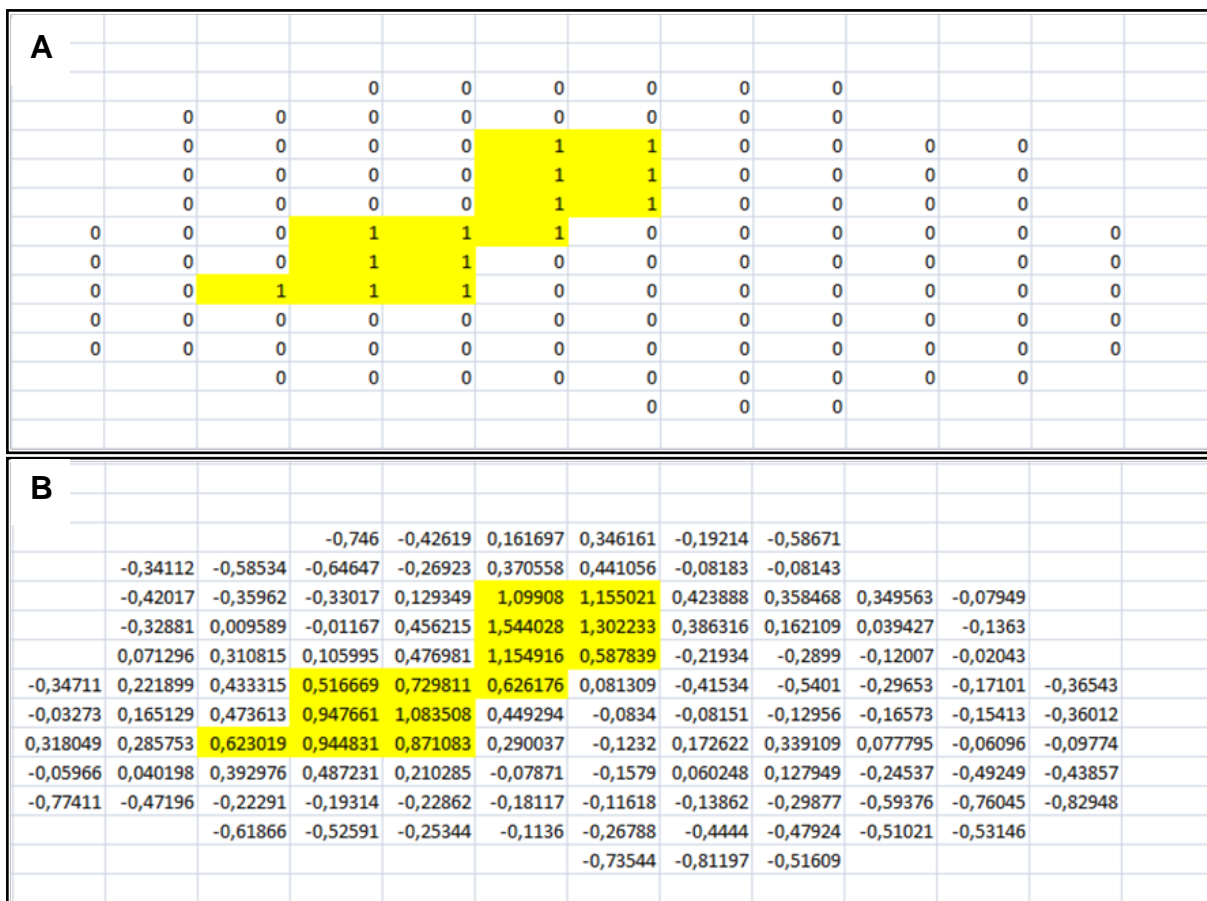


**Figure 6 Identification of MRS-suspicious regions among the MATLAB-export of the voxel values.** Both sheets show the voxels of the same slice as in Figure 5, with the MRS-detected cancer-suspicious region colored in yellow. **A:** All voxels with a smoothed value above the threshold ( $M+SD$ ) are tagged with an "1". A minimum of two directly neighbored voxels with elevated values form a MRS-suspicious region. **B:** Those suspicious regions can then be localized in the Excel sheet containing the precise smoothed voxel values.

MRS-suspicious regions indicating PCa had to be manually identified now. Only a minimum of two directly connected "1"-voxels (not including diagonal neighbors) were considered as tumor regions (Figure 6B). Since the edge voxels might have increased values due to magnetic susceptibility, they were only taken into consideration if at least one direct adjacent voxel, not being located on the slice's margin, had a higher smoothed value. In cases where there were only edge voxels in one suspicious lesion, their spectra were visually inspected. If there appeared to be substantial alteration in the spectra caused by the surrounding fluid, those voxels were not included.

In order to compare the values of MRS-suspicious regions of different prostate samples, a "Malignancy Index" (MI) had been defined within the preliminary study<sup>104</sup>. The MI was defined as the sum of the products of smoothed voxel values (voxel value, VV) and voxel sizes (VS) of a cancer suspicious lesion consisting of n voxels:

$$MI = \sum_{\substack{i=1 \\ VVi > M+SD}}^n (VVi \times VS)$$

The voxel size was constant within one slice and could be calculated based on the measures of the scanned MRS voxel grid.

Apart from the MI, it should be examined whether MRS smoothed values alone (without including the cancer-suspicious lesion size) would give enough information to differentiate suspicious regions that are histologically malignant from those with elevated MRS values but histologically benign structure. The question to be answered was, whether malignant MRS-suspicious regions had higher smoothed voxel values per square millimeter. To address this issue, an Average Voxel Value (Avg) was determined as the sum of the quotients of the smoothed voxel values (VV) divided by the voxel size (VS), and then divided by the number of voxels (n) per lesion:

$$Avg = \left( \sum_{\substack{i=1 \\ VVi > M+SD}}^n (VVi / VS) \right) / n$$

#### **2.3.4 Processing of the histological data**

In order to compare the spectral data with histopathology, the histological slides had to be digitized. Pictures of all slides were taken with a Nikon single reflex camera and all digital pictures were then scaled to the same size of 2200 x 2700 pixels. Using the image editing program GIMP (version 2.8.4), all photos were standardized by manually marking the directions (anterior, posterior, right, left) as well as the estimated middle point of each prostate slice according to the pathologist's tags. Furthermore, the pathologist edged all histologically identified cancer lesions on the glass slide with a dotted line. Those borders of the cancer lesions were digitized as well and their centers tagged in distinct colors (Figure 7).

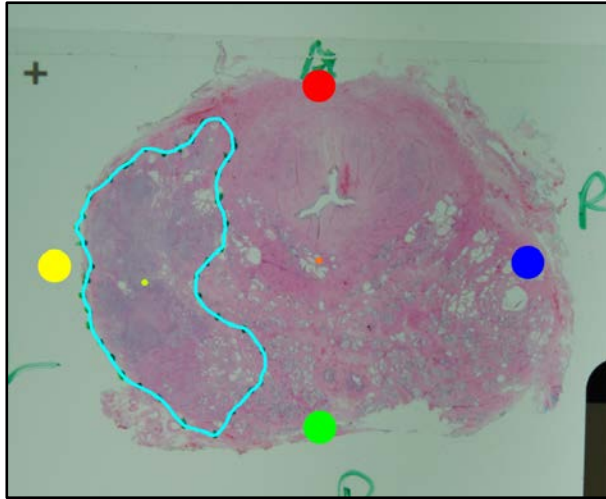


**Figure 7 Standardized picture of a histological slide.** The photo has been scaled, cut and rotated. Furthermore, the directions were marked (anterior: red, posterior: green, right: blue, left: yellow), the histological tumor lesion was circled and its center point tagged in specific colors. Through standardization, the pictures could be analyzed, stacked to a 3D picture of a prostate and later compared with the MRS outcome.

After digitization and standardization the pictures of the histological slices were readily prepared for the alignment with the corresponding voxel grids.

However, further analysis on the histological data needed to be conducted. For planned investigations on histological cancer lesions that were detected by metabolomic imaging versus undetected tumors, two variables were of interest: a) the volumes of the histopathologically detected tumors and b) the distance of a histological tumor center to the middle slice of the prostate or another manually set point. In order to solve this issue, a second MATLAB-based program for a three-dimensional stacking and measurement of the histological data was developed by Yannick Berker<sup>107</sup>. This software converts digitized histological slices into three-dimensional (3D) datasets. The mentioned direction markings, as well as the anatomical shapes enabled a correct alignment of the slides. Moreover, the circled cancer lesions were automatically added up to one 3D tumor region, in case the positions in neighboring slices were comparable. The volume of those cancer regions (in voxels), the coordinates and slice numbers of each 3D tumor region's center, as well as the coordinates of each manual marking were exported into an Excel file. The program additionally calculated the distance (in mm) between a marking and a cancer region's center, plus the distance between a marking and the nearest tumor lesion border.

## **2.4 Analysis: metabolomic imaging versus histopathology**

### **2.4.1 Prior investigation: identification of the corresponding histological middle slides**

The first step to prepare for the comparison of the MRS data with the histopathological outcome was the identification of the histological middle slice corresponding with the acquired MRS/MRI center plane. It was aimed at creating a graph showing a correlate of the histological slice surfaces against the slide numbers, in order to compare this graph with the common shape of a prostate. Thus, a detection of the histological middle slide on the graph was possible.

Therefore, as a correlate for the histological slice surfaces, all the histological slices were traced onto paper for each case, cut out and weighed. Common printing paper with a weight variation of less than 2% among different sheets was used for this step. In order to obtain a parameter which allowed for comparisons among different prostate samples, referred to as "volume percentage", the "paper weights" were then divided by the associated prostate weight after prostatectomy. The weight was used as the divisor since a precise calculation of the whole prostate's volume was not possible whereas the exact prostate weights had been measured after prostatectomy. To verify the use of the weight, a correlation with the approximate volume was determined. Assuming a prostate's shape resembled an ellipsoid, the volume of each sample was calculated using the pathologist's measurements of each gland (length (a), width (b), height (c)) and the common formula of an ellipsoid's volume (V):

$$V = \frac{4}{3} \pi * a * b * c$$

Then, correlation of the estimated prostate volumes and related prostate weights was performed.

In a next step (in order to determine how to identify the histological middle slides), a graph showing the averaged "volume percentages" of the prostate slices from a sample of cases was created. All cases containing seven or eight slides - in total 17 cases (14 cases with seven, three cases with eight slides) - were used. The three cases with eight slides served as a scale for shifting the values of the seven-slide-cases, since it needed to be decided individually (for each case), whether the first slide corresponded with the first or second slide of the eight-slide-cases. Then, the average volume percentage for each slide number was calculated and the data was graphed, with the slide number against the volume percentage. Besides this (average) graph, an individual "volume percentage graph" of each case was created. Using the



information given by the average graph, the middle slide of each prostate specimen was determined based on the individual "volume percentage graphs" (see Results, p. 34).

Finally, it was examined, whether a relevant temporary deformation of the prostate specimen during the MRSI scan had occurred due to gravity, leading to a shift of the middle slice. To examine this issue, a graph showing the average slice surfaces of all 29 slices of five randomly chosen prostate specimens was created and compared with the average "weighted distances" graph of the histological slides as well as the typical prostate shape.

For the calculation of the MRI slice surfaces, the highest and lowest orthogonal diameters for each MRI slice of these selected prostates were measured with the DICOM viewer software OsiriX 3.5 (Figure 8). Since the slices had an ellipsoid border, the diameters (d1, d2) were used to calculate the approximate surface with the common formula for the surface area (A) of an ellipse:

$$A = \pi * \frac{d1}{2} * \frac{d2}{2}$$

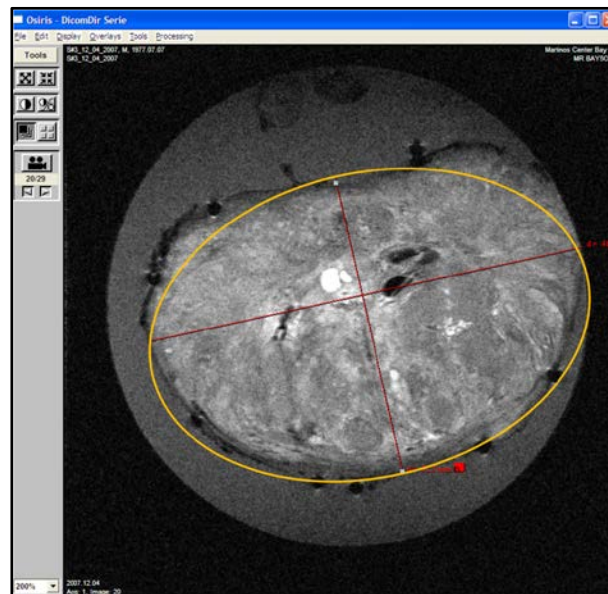


**Figure 8** MRI slice surface area calculation with OsiriX. For five randomly chosen cases, the lowest and highest diameters of each MRI slice were measured and the surface area of an ellipse (roughly including the prostatic tissue, orange line) calculated.

In summary, a technique for the identification of the histological middle slides most exactly corresponding with the MRS central slices was established and tested. Furthermore, an examination of all MRS slices of five randomly chosen cases was performed in order to exclude a relevant compression of the specimens during the scan, which might have effected a shift of the prostates center plane away from the scanner's surface coil.

### 2.4.2 Alignment of MRS and histological middle slice

After identifying the corresponding histological and MRS middle slices, the alignment of histological and MRS slices in order to compare both outcomes was realized.

While the directions of the histological slides were clearly marked by the pathologist, the directions right/left and anterior/posterior had to be recognized among the MRSI slides.

Concerning orientation right/left, the sample holders for the scanning were labeled to ensure a setting that is conventionally applied for cross-sectional imaging. This means that the left side of the picture showed the right part of the sample in MR images and vice versa.

To identify the orientation anterior/posterior, three anatomical structures were compared between histology and the MR image: the whole edge and structure of the prostate, the urethra's shape and position (Figure 9), as well as the location of the seminal vesicles, commonly being located posterior to the prostate's base (Figure 10).

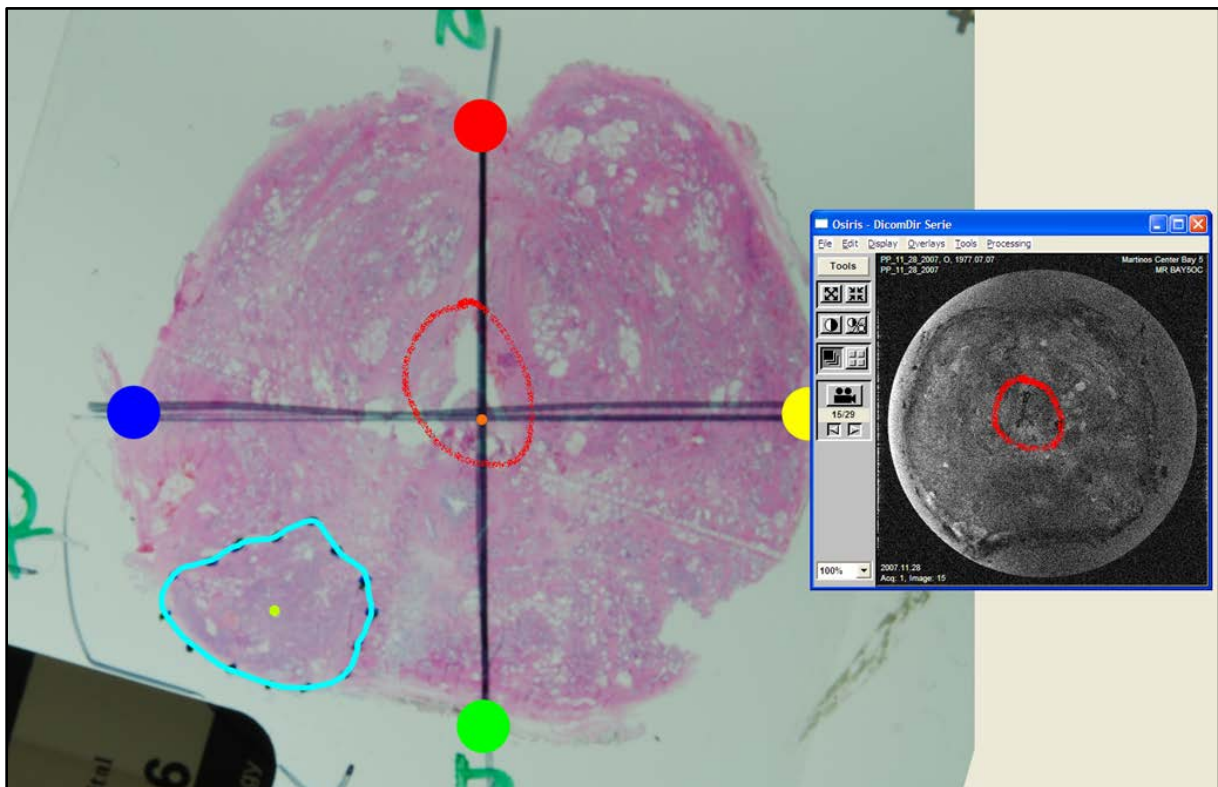


**Figure 9 Identification of anterior/posterior: the urethra's shape.** This histological slide of case 1 shows the anterior orientation (red marking) of the urethra's broadest part. The picture on the right side (OsiriX) presents a MR Image of the same prostate at approximately the same level. The shape of the urethra in MRI clearly equals the histological slide. The top of the MRI acquisitions of this case hence shows the anterior part of the specimen.

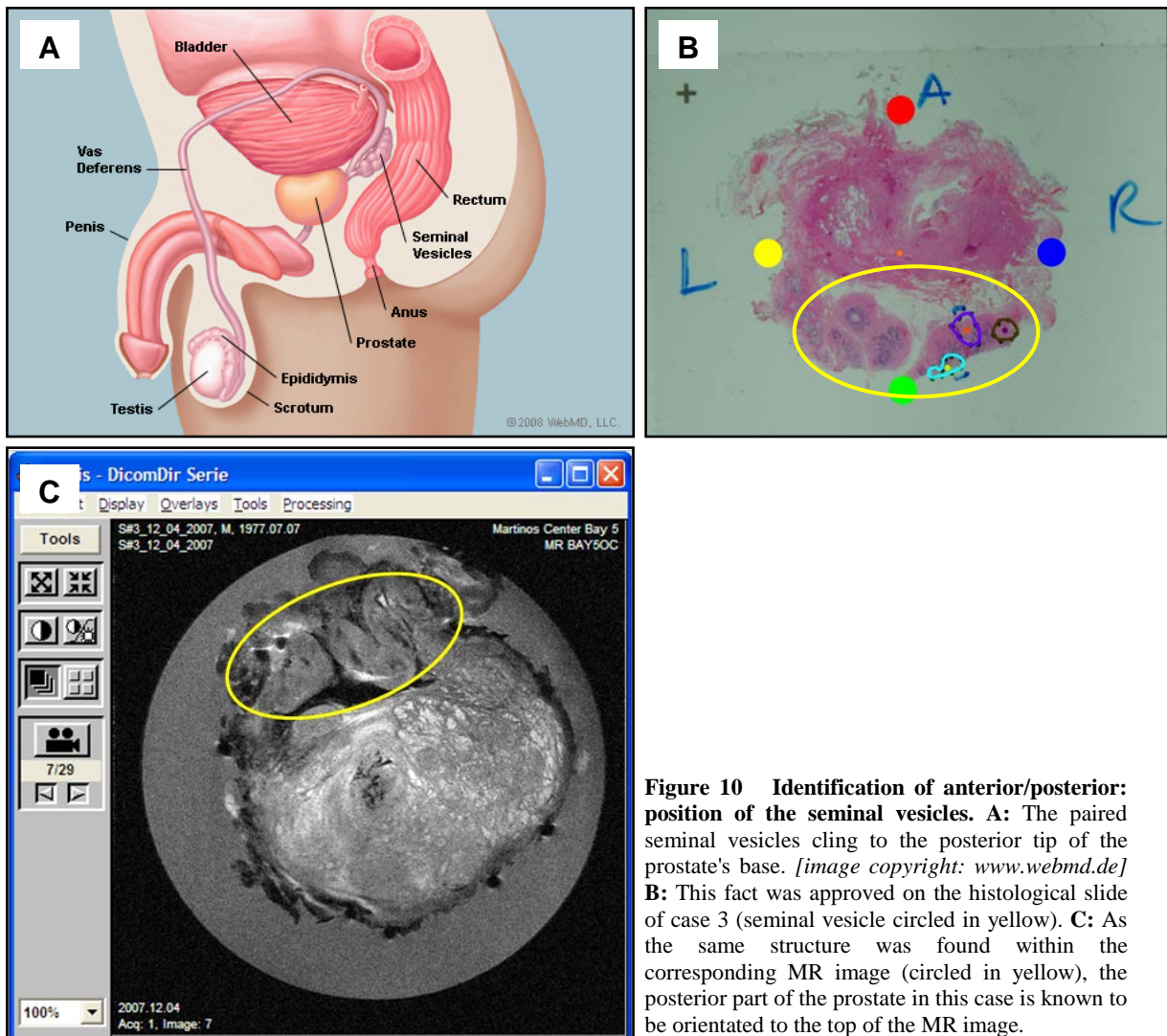


**Figure 10 Identification of anterior/posterior: position of the seminal vesicles.** **A:** The paired seminal vesicles cling to the posterior tip of the prostate's base. [image copyright: www.webmd.de] **B:** This fact was approved on the histological slide of case 3 (seminal vesicle circled in yellow). **C:** As the same structure was found within the corresponding MR image (circled in yellow), the posterior part of the prostate in this case is known to be orientated to the top of the MR image.

With the orientation of both MRI/MRS and histopathology being defined, the actual alignment of the middle slices could be performed using Microsoft PowerPoint. First, a MATLAB snap shot of the overlaying MR image and MRS voxel grid was opened. As the grid often overlapped the prostatic tissue or - in few cases - did not contain all of it, rows or columns were erased or the grid was extended, in order to gain a voxel grid, that would exactly fit the prostate slice of the MR image (Figure 11).

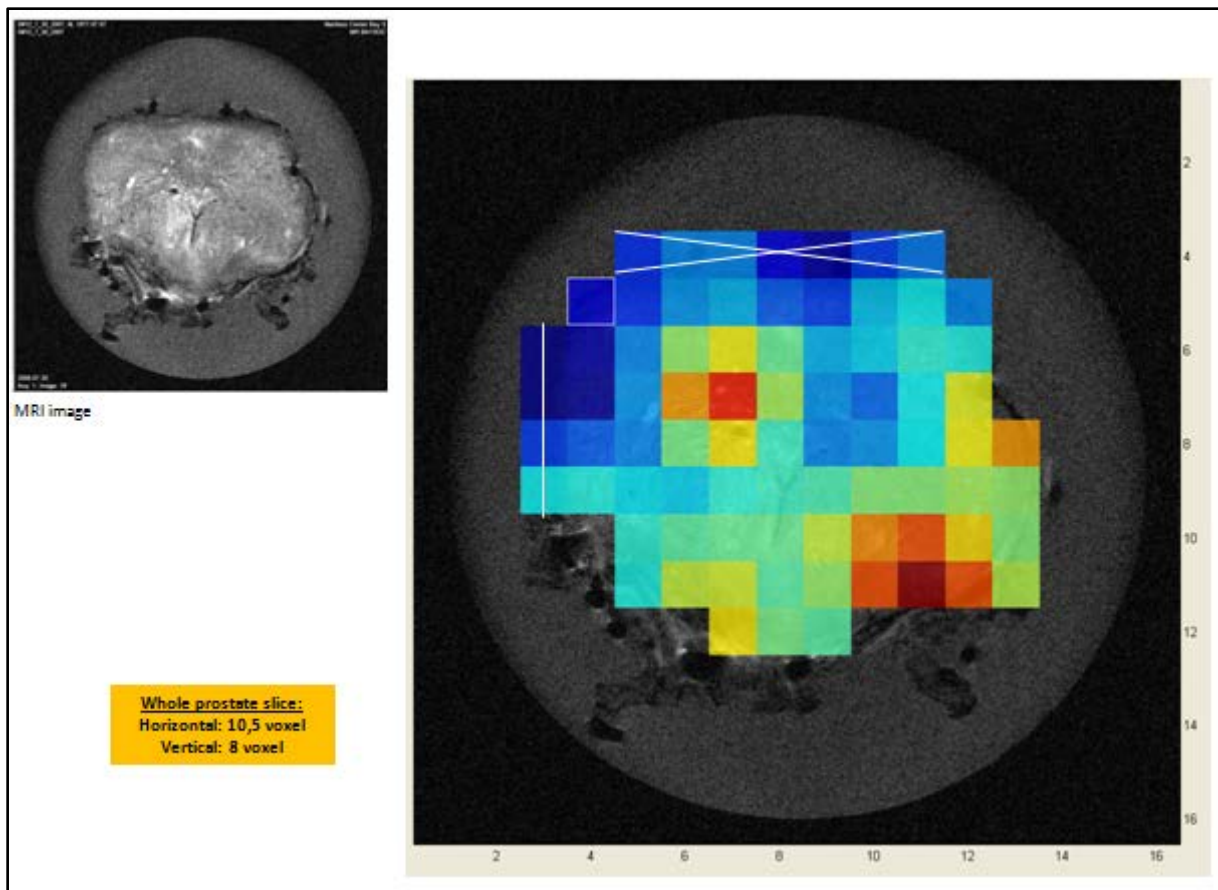


**Figure 11 Adaption of the voxel grid.** In order to create a voxel grid exactly containing the prostatic tissue, rows or columns were added or erased.

This new grid was then copied and the histological picture of the slide was added. Since during the process of embedding and cutting the prostatic tissue samples are known to shrink and slightly deform, the histological slice had to be adapted in order to match the MRS grid. The picture was orientated like the prostate slice in the MR image and then rotated and scaled, until it had the same position relative to the voxel grid of the MR image (Figure 12). Finally, the applicable MRS-suspicious voxels were colored, which enabled a comparison of the histologically defined cancerous lesions with the MRS-suspicious regions in size and location. Whenever a MRS-suspicious region overlapped with a histological cancer lesion or was located less than one directly adjacent or half a diagonally adjacent voxel away from the histological cancer lesion, the MRS-suspicious region was considered as malignant. Otherwise, the MRS-suspicious region did not correspond with a histological cancer lesion and was therefore defined as benign or "MRS false positive" (Figure 13).

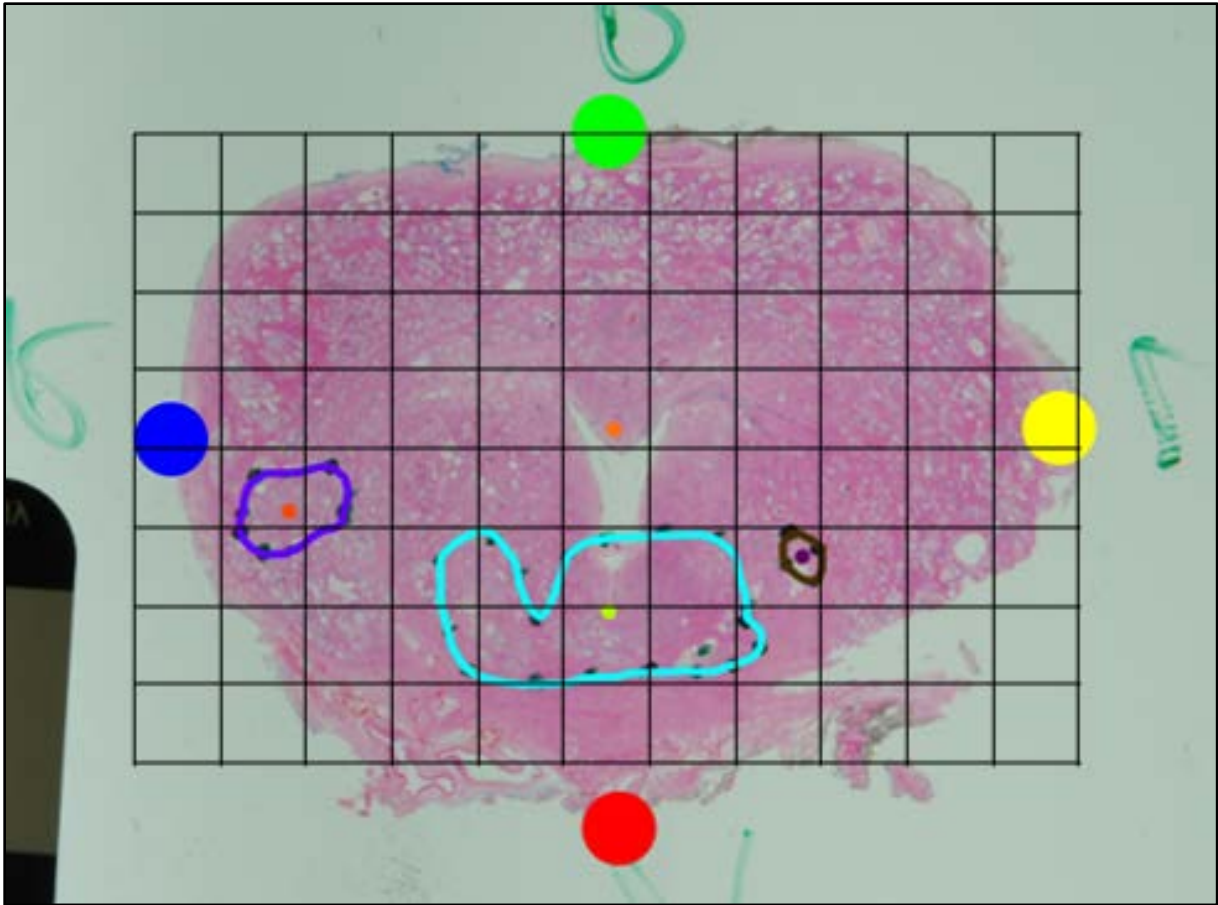


**Figure 12** Adaption of the histological slide. The histological picture was orientated and scaled relative to the voxel grid on the MR image of the same slice in Figure 11. Subsequently, the spectral and histopathological data of the transversal middle slice could be compared.

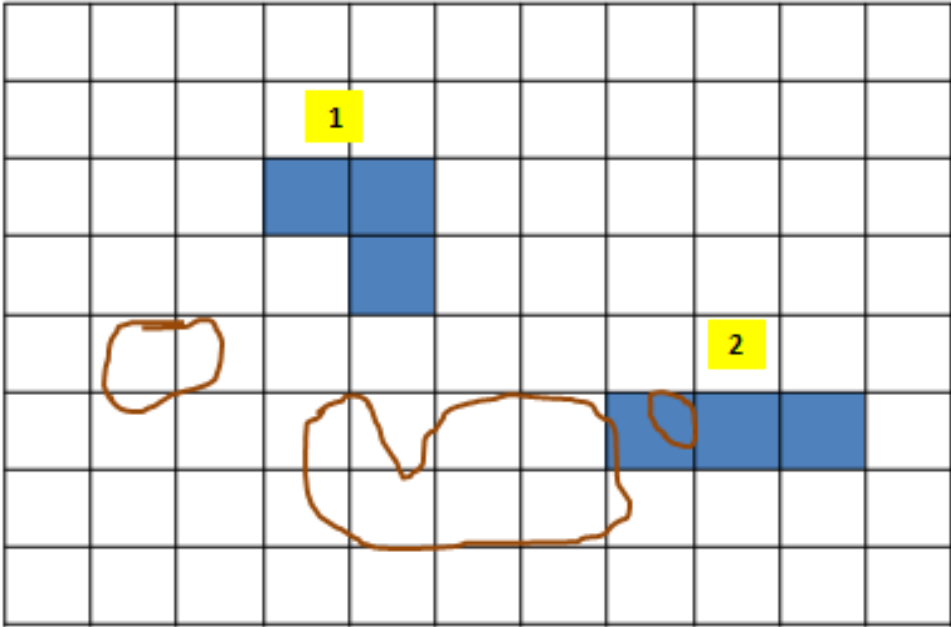


**Figure 13** Comparison between MRS-suspicious lesion and histological tumor region in the same voxel grid. The MRS suspicious voxels are colored in blue, the histological malignant regions circled in brown. Regions overlapping or being less than one adjacent voxel or less than a half diagonal voxel apart, were considered as corresponding regions or histological cancer regions (being detected by MRS). Thus, MRS region 1 did not match with a histological lesion and was defined as histo-benign, whereas MRS region 2 detected two cancerous lesions. The histological malignant region on the left was not detected by MRS.

### **2.4.3 Detection of histological cancer lesions using metabolomic imaging**

As the alignment of MRSI data with the histological outcome was completed, two results were important: the number of histological proven cancer lesions detected by metabolomic imaging, and the amount of MRS-suspicious regions corresponding with a histological cancer lesion and therefore being referred to as "histologically malignant".

After both were quantified, further investigations regarding the MRS-suspicious regions were conducted. It was tested for a potentially significant difference of the Malignancy Index (MI) or the Average Voxel Value (Avg) between the group of MRS-suspicious regions detecting a histological cancer lesion and the group of MRS-suspicious regions being referred to as "histologically benign". The same calculation was performed for the number of voxels of the MRS-suspicious regions.

### **2.4.4 Comparison of detected and undetected cancer lesions**

It was furthermore intended to find characteristics that significantly differed between histological lesions being detected by metabolomic imaging and those not being detected. Therefore it was tested for a possibly significant difference of tumor volume, distance of the histological tumor center to the middle cross-sectional plane of the prostate, Gleason grade or pathological tumor stage between detected and undetected cancer lesions.

The Gleason grade of each individual cancer lesion as well as the pathological tumor stage were identified within the histopathological evaluation. When a lesion had a mixture of two Gleason grades, the pathologist visually estimated the proportion of the different grades to the nearest 10% and a value for the analysis containing both parts was calculated. If a lesion for instance consisted of 80% GG3 cell formations and 20% GG4, the overall GG value was  $0.8*3+0.2*4=3.2$ . The pathological tumor stages occurring within the patient population (pT1c-pT3b) were converted to metric values from 1-6 for the analyses.

The tumor volume for each histological cancer lesion was automatically calculated during the 3D stacking process of the histological slides. The 3D stacking MATLAB-based program was also used to measure the distance between the center of the three-dimensional histological tumor and the histological middle slide (Figure 14, b). The z-coordinates (indicating the height among the prostate specimen) of the middle slide ( $z(ms)$ ), as well as the tumor center ( $z(tc)$ ), were automatically calculated and exported to the Excel file. As the histological slides

were cut in intervals of 5mm, the distance (D) could be calculated using the following formula:

$$D = |z(ms) - z(tc)| \times 5mm$$

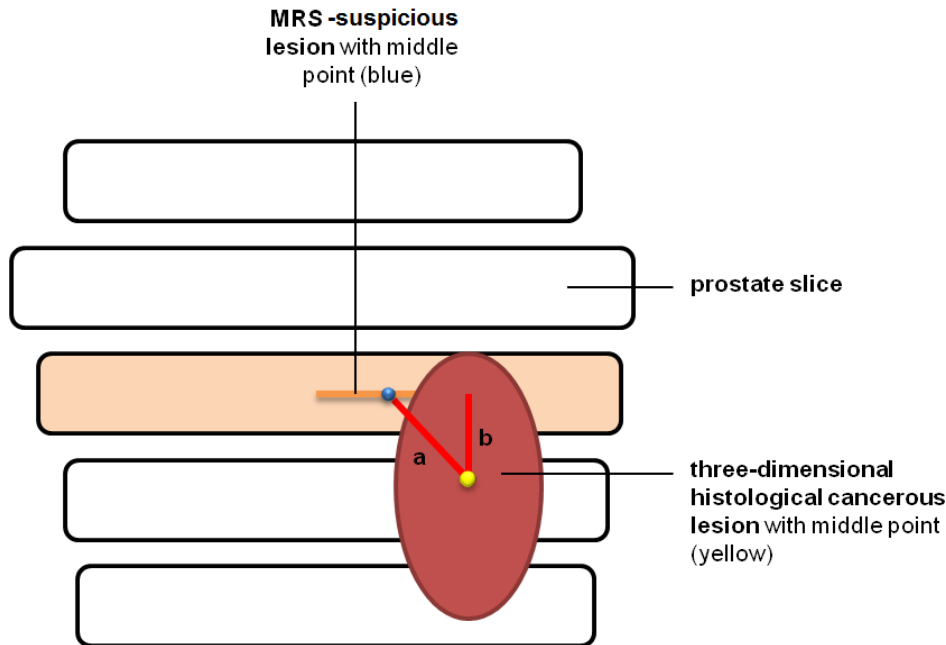


**Figure 14 Distances of interest.** **a:** distance from the MRS-suspicious region center point (blue dot) to the middle point of the corresponding, three-dimensional histological tumor lesion (yellow dot). **b:** gap between the three-dimensional histological tumor lesion's center and the (histological) middle slice.

#### 2.4.5 Prediction of tumor aggressiveness and additional investigations

In order to test how strong the MRSI outcome was in predicting the tumor aggressiveness, parameters of the MRS-suspicious regions (the MI and Avg) were correlated with variables of tumor aggressiveness (the Gleason grades as well as pathological tumor stages of the histological cancer lesions).

Additionally, further investigations on the MRS outcome were performed. It was tested, whether there were any correlations between the MI or Avg and the histological tumor volume or the distance from the MRS-suspicious region middle point to the center of the 3D histological tumor (Figure 14, a). To obtain this distance, the 3D stacking, MATLAB-based program was used. It automatically calculated the referred histological center's coordinates. The middle point of the corresponding MRS-suspicious region had to be manually placed on the digitized histological slice picture before the 3D stacking, in order to obtain the coordinates as well. This process was accomplished with respect to the position of this point in the voxel grid and the overlaying picture of the histological slide. After reloading the

histological pictures with the 3D stacking program, the Excel export would include the distance from this marking to the respective histological tumor center. For the correlation, the absolute distance as well as a "Weighted Distance" were used. The Weighted Distance was calculated as the quotient of the distance divided by the number of voxels of the MRS-suspicious region.

Final analyses were performed among cases where no histological cancer lesion was found on the prostate middle slide. Due to the small number of such cases, only tendencies were described. It was analyzed, whether there were cancer lesions on the adjacent slides and if present, whether the estimated tumor lesion sizes and tumor volumes influenced the height of the MI or Avg of the histologically benign MRS-suspicious regions on the middle slices.

## **2.5 Alternative analysis**

As an alternative analysis, the established analysis protocol described above was applied with one new precondition. The threshold for the metabolomic voxel values referred to as elevated and therefore cancer-suspicious was reduced from  $(M+SD)$  to  $(M+0.75SD)$ .

## **2.6 Statistical analysis**

Statistical analysis was performed with IBM SPSS Statistics 20. For independent groups, t-tests were used and p-values  $< 0.05$  were considered as statistically significant. The testing for normal distribution was performed using the Shapiro-Wilk test (p-value  $> 0.05$ : normal distribution). For variance analysis, the Levene's test was applied (p-value  $> 0.05$ : variances equal).

In case that at least one of the groups did not follow a Gaussian curve or the variances of both groups did not match, the non-parametric Mann-Whitney test replaced the t-test (p-value  $< 0.05$ : statistically significant difference). In order to measure the strength of significant differences or to compare different test results, the effect size (d) was calculated, with  $d \approx 0.2$  indicating a small,  $\approx 0.5$  indicating a medium and  $\approx 0.8$  indicating a large effect, respectively.

Furthermore, correlation analyses were conducted to reveal relationships between two metric groups. Normal distribution had to be tested for, using the Shapiro-Wilk test. For normally distributed groups, Pearson's correlation was performed, and Spearman's correlation if there



was no normal distribution of values. In both tests, a p-value  $< 0.05$  was indicated a significant correlation, whereas values between 0.05 and 0.1 were considered as a tendency. In case of statistical significance, the correlation coefficient revealed the type of correlation (positive or negative) and could be used to compare the effect sizes.

### **3. Results**

#### **3.1 Prior investigation: identification of the corresponding histological middle slides**

For the identification of histological middle slides, a graph was created where a correlate of the histological slice surfaces was plotted against the slide numbers. Here, the "volume percentage", which is the quotient of the paper weight of a histological prostate slice divided by the weight of the whole prostate, served as the correlate of the histological slice surfaces. In order to approve the application of the specimen weight instead of its volume, both parameters were correlated. As a result, a positive correlation ( $p = 0.01$ ) was found, meaning that the usage of the weight for the "volume percentage" was appropriate.

To identify the middle slides, a consideration of the prostate's anatomy was inevitable. Prostates commonly are oval shaped with a rounded tip. The transverse slices with highest diameter and hence maximum surface area are located close to the center plane, but are slightly shifted towards the base of the prostate, as this end is wider than the apex (Figure 23, appendix p. 73).

The average graph demonstrating the "volume percentages" of the prostate slides of the 17 analyzed cases was compared to the typical prostate shape. It showed a steady increase of the "volume percentage", which reached its peak shortly after the middle of all slides and then decreased, forming an unfinished u-shape (Figure 15). As the slides had been cut from the apex to the base, this course of the curve supported our suggestion that the middle slice reached a "volume percentage" close to the peak.

In order to identify the histological slide closest to the middle cross-sectional plane of the prostate, the histological slide next to the peak of the "volume percentage" had to be chosen. Thus, the individual "volume percentage" graph of each case was created and the middle slide of this case determined (Figure 16).

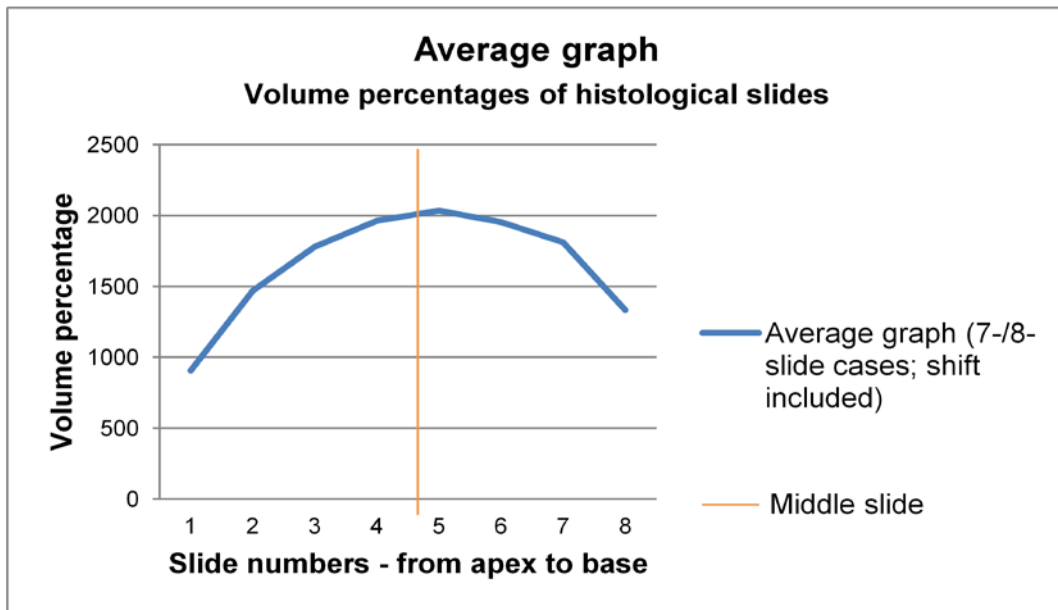


**Figure 15** Graph of the average volume percentages of all seven- and eight-slide cases. The transverse slice with the highest diameter and surface area is located close to the middle cross-sectional plane, but shifted towards the base of the prostate. For the identification of each case's middle slide, the slide with the highest volume percentage right before the peak value has to be chosen (orange line).

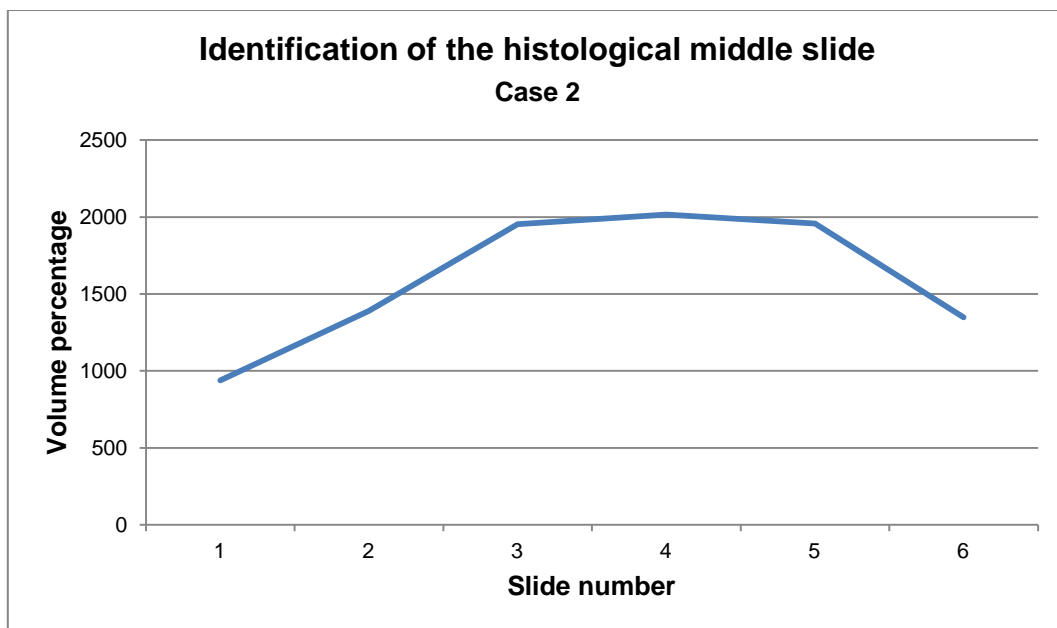


**Figure 16** Identification of the histological middle slide - case 2. As the middle slide is proven to reach a volume percentage close to the peak, slide number 3 was determined as middle slide for this case.

Furthermore, the MRSI data were examined to exclude a temporary compression of the prostate specimen due to gravity during the scan (probably resulting in a shift of the middle slice). A visual comparison of the graph showing the 29 MRSI slices of five randomly chosen cases against the slice numbers with the average "weighted distances" graph of the histological slides revealed a similar course of the curves (Figure 17). Thus, the surfaces of the slices and their relation did not significantly differ between the MR images and

histological slices. Hence, it was assumed that no relevant deformation of the tissue occurred during the scan, and the MRI/MRS middle slice had not been shifted.

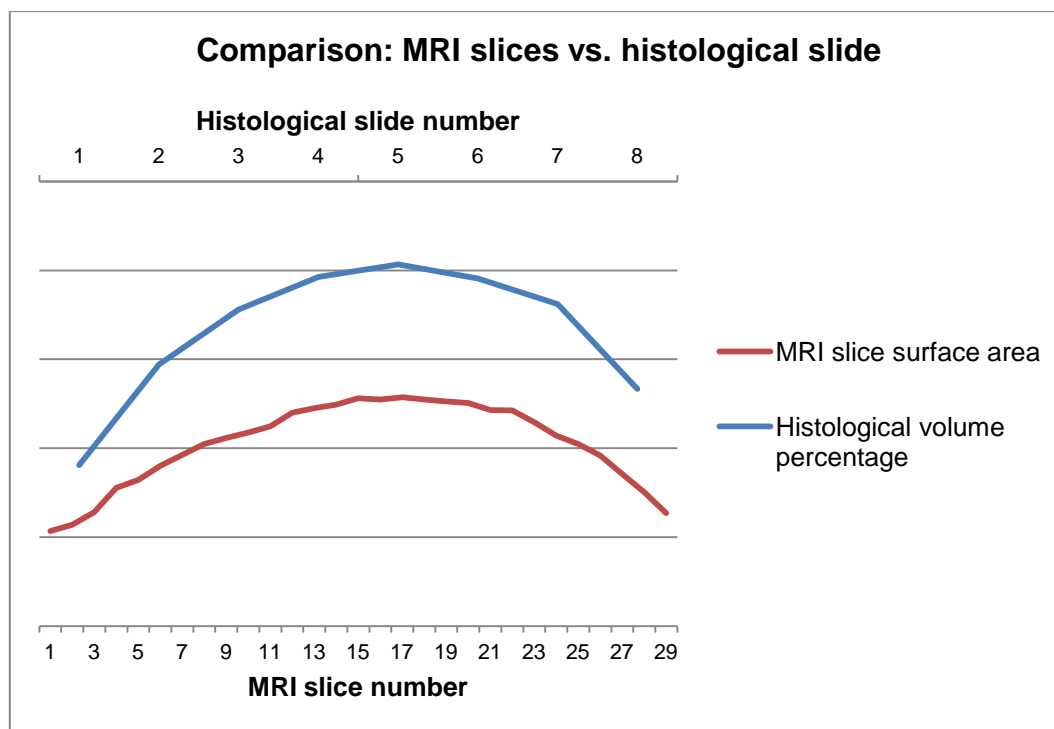


**Figure 17 Comparison of MRI average slice surface areas and average histological slide volume percentages.** This graph shows the average MRI slice surfaces per slice (red) as well as the average "volume percentage", demonstrating the correlate of the average surface areas for each histological slide number (blue). The figure reveals a similar course of both curves. Thus, no relevant deformation of the specimen during the scan had occurred due to gravity.

### 3.2 Objective 1

#### 3.2.1 Cancer detection using metabolomic imaging

For the middle slides of the 30 examined cases, MRS revealed 69 suspicious regions whereas the pathologist identified 46 histological cancer lesions. After aligning the corresponding MRS slices and histological slides, 61% of the histological regions on the middle slices (28 out of 46) were found to be detected by MRS. Consideration of the three-dimensional information of the histological tumors increased the MRSI detection rate to 67% (26 out of 39 three-dimensional tumors), as some of the lesions on a slide belonged to the same 3D tumor. Overall, the metabolomic maps accurately identified 18 of the prostates as being cancerous. Since six samples did not contain histological cancer regions on the middle slide, these 18 cases represent 75% of the samples showing cancer lesions on the examined slice. After inclusion of these six cases into the analysis, 60% of all prostates were detected as cancerous by only evaluating the middle cross-sectional planes.

The detection rate of the histological cancer lesion on the middle slides varied among specimens with different Gleason scores - the higher the Gleason score, the more accurate the detection. With regards to Gleason score, rates of 45% (GS 3+3, 12 samples), 71% (GS 3+4, 14 samples) and 75% (GS 4+4, 4 samples) were ascertained.

Out of the 69 MRS-suspicious regions, 26 corresponded with a histological tumor lesion and were subsequently considered as malignant. In contrast, 43 MRS-suspicious regions occurred without histopathological counterpart and hence were determined to be benign, emerging as "MRS false positives".

It was tested whether suspicious MRS regions that actually corresponded with malignancy (based on the histopathology) could be distinguished from benign regions on the basis of the Malignancy Index (MI). A significant difference of the MI between malignant and benign MRS regions was shown, with cancerous regions having significantly higher MI values ( $p = 0.006$ , effect size: 0.61). The ROC curve of the MI indicated an overall accuracy of 70% to differentiate between malignant and benign MRS-suspicious regions (Figure 18). For a full list of the coordinates see Table 5 (Appendix, p. 76).

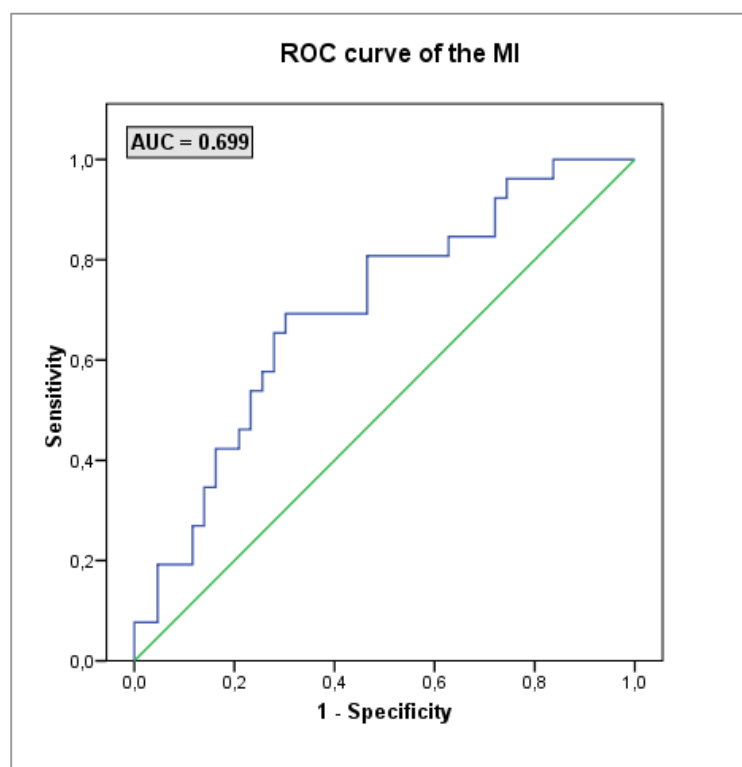


**Figure 18** ROC curve of the MI. An area under the curve (AUC) of 0.699 was shown for the differentiation between malignant and benign MRS-suspicious regions. Consequently, the MI proved to have a diagnostic accuracy of 70%.

The same analysis was performed for the Average Voxel Value (Avg). No significant difference in Avg between malignant and benign MRS regions was obtained ( $p = 0.134$ ).

Due to the fact that those results indicated an important role of the MRS-suspicious region size (which has a large impact in the calculation of the Malignancy Index), the number of voxels forming such a region became a part of the analysis. The t-test showed a significantly higher voxel number (and therefore larger lesion size) for MRS-suspicious regions being considered as malignant ( $p = 0.019$ , effect size: 0.45).

In summary, 75% of the cases with a histological cancer lesion on the middle slide were identified as cancerous by metabolomic imaging. The MI as well as average voxel number showed to be parameters that may significantly differentiate between MRS-suspicious regions corresponding with a histological tumor and those occurring as false positives, whereas the Avg did not show a significant difference.

### **3.2.2 Differences between detected and undetected cancer lesions**

No significant difference was found between both groups regarding tumor volume ( $p = 0.280$ ), distance from the histological 3D tumor center point to the middle slide ( $p = 0.332$ ), pathological tumor stage ( $p = 0.414$ ), and Gleason grade of the histological lesion ( $p = 0.180$ ).

## **3.3 Objective 2**

### **3.3.1 Estimation of tumor aggressiveness**

A positive correlation between MI and GG ( $p = 0.021$ , correlation coefficient = 0.406) was found, whereas the MI negatively correlated with the pT ( $p = 0.038$ , correlation coefficient = -0.368). The Avg neither correlated with the GG ( $p = 0.348$ ) nor with the pT ( $p = 0.726$ ).

### **3.3.2 Additional findings**

There was no correlation among the tumor volume and Avg ( $p = 0.426$ ). The same result was obtained for the volume and MI. However, the p-value of 0.060 with a correlation coefficient of 0.336 displayed a tendency for higher tumor volumes inducing higher MIs.

While there was no correlation between MI and the absolute distance ( $p = 0.248$ ), a negative correlation between MI and the Weighted Distance was obtained ( $p = 0.000$ , correlation

coefficient = -0.700), with lower Weighted Distances inducing higher MI values. Similar results were demonstrated for the Avg, which did not significantly correlate with the absolute distance ( $p = 0.069$ , correlation coefficient = -0.326), but showed a tendency for an inverse relation. Moreover, a significant negative correlation among Avg and Weighted distance was obtained ( $p = 0.012$ , correlation coefficient = -0.437).

Further investigations on the cases without histological malignant lesions on the middle slide were conducted. Six out of the 30 cancerous samples complied with this criterion. Due to this relatively small number, only tendencies were described. The samples could be divided into two groups: four of them had at least one slide next to the middle slide with a malignant lesion, whereas two samples did not have this feature. Those adjacent lesions were then visually judged on a size scale, ranging from S (small), M (medium) to L (large). Moreover, the histopathological volumes of the whole tumors were compared, as well as the average MI and Avg of all MRS-suspicious regions of the middle slide (Table 3).

Case #	Middle slide	Slides with histological tumors	Adjacent slide with tumor?	Average MI	Average Avg	Size of histological tumor lesion	Volume of histological tumor
4	2	1	Y	42.60	0.12	S	23052
5	4	1, 2, 3	Y	27.59	0.05	2 x S	29736, 7053
9	3	1, 2	Y	72.84	0.07	M - L	611231
14	3	6	N	43.86	0.06	-	-
24	4	3, 5	Y	166.96	0.06	2 x M	68691, 39261
28	5	2	N	31.97	0.05	-	-

**Table 3 Cases without a histological tumor lesion on the middle slide.** Cases without a malignant lesion on an adjacent slide are colored in grey. The MI and Avg values were calculated as the average of all values of the MRS suspicious lesions on the middle slide. The histological cancer lesion size was visually scaled. Y = yes, N = no, S = small, M = medium, L = large. Volume given in voxels.

The mean of the average MIs of the cases with a malignant histological lesion on a slide next to the middle slide was 77.50, compared to 37.92 in the second group consisting of two samples. The mean of the Avg of the cases with adjacent malignant lesions was 0.08, and 0.055 in the other group, respectively. Within the group of cases with a cancer lesion on an adjacent slide, cases 4 and 5 achieved the lowest average MIs and also showed the smallest lesion size and tumor volumes.

In summary, the six cases without a histological tumor on the examined middle slide revealed smaller mean MI and Avg values for samples without a histological tumor on the slides next to the middle slide.

### 3.4 Objective 3: alternative analysis

As MRS did not detect all histologically malignant lesions within the settings above, the threshold for the smoothed MRS voxel values (considered as being elevated and therefore suspicious) was lowered from  $(M+SD)$  to  $(M+0.75SD)$ . Consequently, 74 MRS-suspicious regions were identified - five more compared to the original threshold. Out of 46 histological tumor lesions on the middle slide, 72% were detected by MRSI, representing 77% of the three-dimensional tumors. Furthermore, 83% of the cases with histological tumors on the examined slice were identified as cancerous - two cases more than in the original analysis. Finally, 31 MRS-suspicious regions (42%) indeed detected a histological tumor lesion, whereas 43 (58%) were benign. In the original analysis, 26 MRS-suspicious regions were malignant and 43 benign. This finding means that all the additional MRS-suspicious regions with metabolomic voxel profile values above the lower threshold successfully detected a histological cancer lesion.

It was then tested whether MI, Avg or number of voxels of the MRS regions could differentiate between cancer and benign MRS regions. Surprisingly, neither the MI ( $p = 0.066$ ), nor the number of voxels ( $p = 0.157$ ) could differentiate between MRS-suspicious regions detecting real tumors from benign regions. The same result was obtained for the Avg ( $p = 0.820$ ). Therefore, no further analysis was performed.



## **4. Discussion**

### **4.1 Interpretation of the principal findings**

The present study was designed to further test the metabolomic PCa profile implemented within the preliminary in-lab study. Therefore, two essential changes among the study design were successfully integrated. First, the sample size was increased from 5 to 30 whole prostates. Second, a partial automation of the processing and analysis procedure was performed. In contrast to the former workflow, the import of the MRS and MRI data as well as the alignment of both, the preprocessing, Profile Fitting and the data export were now automated tasks<sup>107</sup>. Consequently, an impressive reduction of the time frame from more than a month to 14-16 hours per case was achieved.

#### **4.1.1 Original analysis**

The study followed three major objectives. As a primary objective, the metabolomic imaging technique was tested regarding its capability to detect cancer lesions identified by histopathology. 61% of the histological cancer lesions on the middle slides of the prostates were detected by MRSI, leaving room for further improvement. Apart from this, 18 of the 30 prostates (60%) were identified as cancerous. This still includes the six cases without histological cancer lesions on the middle slide that were impossible to be identified as malignant by only analyzing this single plane. With those cases excluded, the percentage of detected cases increases to 75%. A solution to this problem would be to add more prostate slides to the metabolomic analysis, with the subsequent effect of raising the time frame for processing and analysis.

It was furthermore examined, whether the variables Malignancy Index (MI) and Average Voxel Value (Avg) could significantly differentiate between the MRS cancer-suspicious regions corresponding with a histological PCa lesion from the MRS false positives. The MI already demonstrated its great potential to detect the truly malignant MRS-suspicious regions in the preliminary study. With the Avg, another parameter was added in order to investigate whether also the Average Voxel Value of a MRS-suspicious regions (without the influence of the voxel number) significantly differed among malignant and benign MRS-suspicious regions. The associated hypothesis was that MRS-suspicious regions that corresponded with a histological cancer lesion had significantly higher MI and Avg values than the benign regions.

Regarding the MI, this hypothesis can be confirmed. With a diagnostic accuracy of 70%, it again proved the promising potential to identify malignant MRS-suspicious regions. Depending on the MI cut-off value being chosen for future diagnostic tests, the sensitivity as well as specificity of the MI to differentiate between malignant and benign MRS-suspicious regions varies. According to the coordinates of the corresponding ROC curve (Table 5, Appendix, p. 76), the highest values for both parameters are obtained with a MI cut-off value of 45.87. Here, a sensitivity of 69% and a specificity of 70% are achieved. The choice of a lower MI cut-off value would result in higher sensitivity levels (however at an expense of a lower specificity), which might be required for a screening test.

In contrast to the MI, the Avg did not significantly differ between both groups. This fact indicated an important role of the region size and therefore number of voxels that form a MRS-suspicious region in the process of eliminating false positives. Due to this finding, another parameter was included into the analysis: the number of voxels that generate a MRS-suspicious region. As expected, a significant difference of this number between malignant and benign regions was found. However, with an effect size of 0.45, the strength of this variable could not reach the MI (effect size = 0.61).

The conclusion is that with the help of the metabolomic imaging technique, histologically proven PCa lesions can successfully be identified. Nevertheless it needs to be discussed, how the detection rate may be improved. Apart from this, the MI again proved to be a solid tool to differentiate MRS-suspicious regions of malignant nature from false positives. Especially the inclusion of the region size into this variable seems to be crucial. This leads to the assumption that small cancer lesions are harder to detect. Finally, it was found that a notable number of voxels with elevated and therefore suspicious metabolomic values appear within histologically benign tissue regions.

The results discussed above raise two principal questions: First, why do some of the histological cancer lesions remain undetected? Secondly, why do MRS-suspicious regions of histologically benign nature - referred to as "false positives" - appear?

Regarding the first question, it was hypothesized that non-detected tumors were of lower volume and/or lower aggressiveness (resulting in lower Gleason grades and pathological tumor stages); furthermore, their 3D centers were located further away from the analyzed prostate middle slide. Surprisingly, these expectations could not be confirmed: detected and undetected tumor lesions did not significantly differ in any of those features. Consequently,

the question why some tumors were not detected cannot be answered sufficiently at this point. It can only be assumed that differences in volume, tumor aggressiveness and/or distance to the middle slice may become statistically significant if a larger sample size with more diverse Gleason grades and pathological tumor stages is analyzed.

Considering the second question, with 43 of 69 MRS-suspicious regions in total, 62% were identified as histologically benign and thus MRS false positive. Exactly the same percentage has been described in the preliminary study. At present, it cannot be sufficiently explained, why false positives occur in such a high number. Further in-lab research (unpublished data, manuscript in review) suggests the existence of "metabolomic field effects" leading to cancer-specific metabolic changes even among non-neoplastic cells in prostates with PCa. The occurrence of benign voxels with still elevated metabolomic profile values (referred to as false positives) within the current study supports this hypothesis.

The secondary objective of the present study was the prediction of tumor aggressiveness. It was hypothesized, that the MRSI outcome (MI, Avg) significantly correlated with markers of tumor aggressiveness (Gleason grade, pathological T-stage), leading to higher MI and Avg values in aggressive tumors. The MI met this hypothesis: it showed a positive correlation with the GG of medium strength (correlation coefficient: 0.406). The correlation coefficient may rise with a higher sample size. In contrast, the surprisingly negative correlation with the pathological T-stage (correlation coefficient: -0.368) remains elusive. As there was a low variety of different pathological T-stages among the patient population (53% of the prostate specimens were of pT2c), this outcome is suspected to be coincidental. Unlike the MI, the Avg does not work as a predictor of tumor aggressiveness. This fact was not unexpected, after the inability to differentiate between malignant and benign MRS regions had been demonstrated before.

In summary, the aim to predict tumor aggressiveness with the help of the MRSI outcome was achieved and could probably be further supported using a larger sample size.

Further investigations on the malignant MRS-suspicious regions were performed for a better understanding of the MRSI technique. The associated hypothesis was that the MRSI outcome would be influenced by tumor features like the volume or the Weighted Distance from the 3D tumor center to the MRS region middle point, with higher volumes and lower distances inducing higher MI and Avg values. A tendency of higher tumor volumes being connected to elevated MI values could be shown. This can be explained by the fact that larger tumor

lesions come along with larger MRS-suspicious regions resulting in higher MIs. Regarding the distance, a lack of a significant correlation between MI or Avg and the absolute distance from the histological 3D tumor center to the MRS region middle point was shown. This can be explained by the fact that the centers of very large 3D histological tumors can be located quite far from the prostate middle slide including the MRS-suspicious region, although the histological tumor cuts this middle slide. In order to address this problem, the Weighted Distance, which is the absolute distance normalized by the number of voxels included, was introduced in the preliminary study. As hypothesized, a negative correlation between WD and MI (correlation coefficient: -0.700) and even between the WD and Avg (correlation coefficient: -0.437) was shown. Thus, tumors being located close to the middle slide induce a higher MRS signal.

A challenge within this study were the six cases without a cancer lesion on the histological middle slide. On the one hand, they could not be detected as cancerous with this method. On the other hand, in all of the six cases MRS false positives occurred. There was a tendency that MRS false positives had higher MI and Avg values, if tumor lesions on an adjacent slide were present. The larger the volume of those histological tumor lesions on the adjacent slide, the higher the MI and Avg values. This fact did not improve the detection rate. In contrast, it even weakens the MI. However, the results regarding those six cases provide a better understanding of metabolomics among PCa and further support the theory of metabolomic field effects.

#### **4.1.2 Alternative analysis**

Within the preliminary study, it was found that the metabolomic profile values of all histologically benign voxels fell under the threshold of  $(M+SD)$  of a respective prostate plane<sup>104</sup>. Therefore, this empirical value was used in order to define the malignancy-suspicious MRS voxels within the voxel grid. However, as shown in Figure 22 (see Appendix, p. 72), not all malignant voxels had a voxel value above this threshold within the preliminary findings. This might be the main reason for a relatively high number of histological PCa lesions that stayed undetected in the present study.

Consequently, it was hypothesized that a reduction of the threshold to  $(M+0.75SD)$  would lead to a higher detection rate of cancer lesions. Nevertheless, this adaption of the threshold was also expected to result in a higher number of MRS benign regions (false positives) as well as a lowered strength of the MI and Avg.

Our hypothesis was supported in terms of the detection rate. An additional five histologically proven cancer lesions could be identified, increasing the detection rate from former 61% to 72%. Moreover, two more cases were identified as cancerous, meaning that 83% - rather than 75% within the original analysis - of the prostate specimen with a cancer lesion on the middle slide were found to be affected. A promising fact was that (against the expectations) no further false positive MRS-suspicious regions appeared.

The essential difficulty was the MI. With the lower threshold of  $(M+0.75SD)$ , the MI did not significantly differentiate the malignant MRS-suspicious regions that corresponded with a histological cancer lesion, from the benign lesions. In consequence, although more PCa lesions were detected, the method is not useful without a strong MI, as false positives cannot be eliminated.

In summary, it is important for metabolomic imaging to find a voxel value threshold that keeps an acceptable balance between a slightly lowered cancer detection rate and a strong MI to identify the false positives. It was shown that  $(M+SD)$  serves as a more successful threshold. However, the lower threshold of  $(M+0.75SD)$  with a considerably higher detection rate may be promising in the context of a non-invasive PCa screening, since a high sensitivity (however low specificity) can be expected.

#### **4.2 Principal findings in the context of current literature**

As described above, compared to the preliminary study the time duration of the metabolomic imaging method was successfully improved through partly automating the processing and analysis process. However, regarding the MI, the results of the preliminary study could not be confirmed at such a high level. In the preliminary study, an overall accuracy of 93% (all tumors) to 97% (only pT2 tumors) for the MI had been shown. As only five whole prostates, of which four were of pT2 and one of pT3, had been included into that study, the high accuracy of the method was discussed to be potentially overestimated and considerably shifted towards pT2 tumors<sup>104</sup>. This assumption was confirmed within the present study. Here, the MI demonstrated an accuracy of only 70% to differentiate between malignant and benign MRS-suspicious regions.

Another finding of the preliminary study was a significant positive correlation between the MI and histological tumor volume as well as a significant inverse correlation between the MI and the Weighted Distance among the pT2 specimen. These findings were reaffirmed for the

cancer lesions of all pathological tumor stages within the present study. Investigations on the prediction of tumor aggressiveness were not part of the preliminary study.

The application of a whole metabolomic profile connected with the MRSI technique is a fully new approach among PCa diagnostic research. Hence, no further studies using the same mechanism were found in the pubmed database.

A similar technique is the previously introduced MRSI method using the metabolite ratio  $(C+C)/C$ , rather than the information of the whole metabolome (see Introduction, p. 6). In a meta-analysis performed by Wang et al., a pooled weighted sensitivity of 82% in PCa detection had been assessed<sup>95</sup>. With a detection rate of 75% (including only the prostates with a cancer lesion on the middle slide), the metabolomic technique of the present study did not yet reach the same accuracy. However, the same weakness in detecting low-grade tumors was demonstrated. The detection rates for malignancies with different Gleason scores showed clear similarities with the outcome of the  $(C+C)/C$  ratio: the rate was 45% for tumors of GS 3+3 ( $(C+C)/C$ : 44%), 71% for GS 3+4 ( $(C+C)/C$ : 77%) and 75% for GS 4+4 ( $(C+C)/C$ : 90%)<sup>100</sup>. Apart from this, both methods demonstrated their feasibility to predict tumor aggressiveness, as a positive correlation between MRSI outcome and Gleason grade or Gleason score was shown. While Zakian et al. found a sensitivity of 81% for the  $(C+C)/C$  outcome to classify cancer lesions as low- or high-grade, in the present study no further testing regarding this issue was performed<sup>100</sup>.

Another similar approach is the expanding research on PCa metabolomics in blood sera. As a notable difference, only the technique of MRS is used within those studies, as MRSI is not necessary<sup>108,109,110</sup>. Promising results were obtained by Kumar et al., who quantified 52 metabolites among the filtered sera of 210 patients<sup>110</sup>. Samples of healthy patients were distinguished from samples of patients with PCa with a sensitivity of 99.9% and a specificity of 94.7%. This method seems to have a great potential to be implemented in the clinic as a diagnostic tool. In contrast to metabolomic imaging, it is neither possible to stage the tumor nor to guide biopsy using this method.

In summary, many similarities between metabolomic imaging and other techniques such as the  $(C+C)/C$  ratio or the MRS analysis of blood sera were found. However, further research is necessary in order to increase the PCa detection rate.

### **4.3 Limitations of the study**

Having discussed the principal findings of this study in the context of current literature, several limitations cannot go unmentioned. Three major shortcomings of the study were identified: the patient population as well as the spectral processing and the alignment with the histopathological outcome.

#### **4.3.1 Patient population**

An essential limitation was the patient population included in our study.

First, a higher sample size needs to be included in future studies. This would eventually lead to more significant results, especially regarding differences between detected and undetected tumor lesions.

Secondly, a higher variation regarding pathological tumor stage and Gleason scores needs to be included. In the present study, 90% of the cases were of pT2, while there were only one pT1 and two pT3 prostate specimens. Samples of pT4 were not part of the patient population. Consequently, the results are possibly shifted towards pT2 tumors. The Gleason scores were of higher variation (40% GS 3+3, 47% GS 3+4, 13% GS 4+4). However, a bias clearly exists, as no samples of GS 4+3 were included.

Thirdly, it is important to emphasize that only cancerous prostates were examined within this study, since it is ethically impossible to perform prostatectomy on healthy men. Therefore, no real control group exists, which might be important since the metabolomic values of benign prostatic regions of cancerous prostates might be elevated due to the formerly discussed field effects. It is of high interest, whether the metabolomic values in tissue of cancer-free prostates are lower and whether it would thus be necessary to adjust the threshold between malignant and benign metabolomic values.

#### **4.3.2 Spectral processing**

Further limitations of the present study were identified among the process of spectral correction and analysis as well as for the Profile Fitting.

Most importantly, a metabolomic PCa profile obtained with a 14T MRS scanner was applied to the 7T MRS data during the Profile Fitting. Due to the different spectral resolutions of both datasets, it would be of high interest to develop a metabolomic PCa profile with a 7T scanner and apply it to the spectra of the 30 prostate middle slides of this study.

Furthermore, metabolomic imaging is technically challenging, time-consuming, and thus expensive. Even though partial automation was achieved for the process, there are still time-intensive manual processing steps, which make the spectral processing a potentially subjective, user-dependent and not a one hundred percent-reproducible task. In the present study, a consistent standard within the spectral processing was maintained, since the whole process was performed by one person only. However, with a full automation the processing would be expected to be more reliable and faster for a clinical implementation. Additionally, more cross-sectional planes could be integrated into the analysis.

Before a higher grade of automation is realized, it is recommendable to first test the accuracy of the automatically processed spectra by comparing the outcome with fully manually corrected spectra. An option would be to re-process some of the cases included in the present study with the manual tool NUTS (which was used for the preliminary study), and to compare the results.

Additional minor limitations are difficult to prevent in further studies. During the scan of the prostates, different fields of view - depending on the gland size - were used. As the voxel size is an important variable in the calculation of the MI, different values may have an impact on the MI. This phenomenon is especially suspected among voxels that contain both cancerous and benign tissue. Moreover, voxels with a mixture of malignant and benign information especially occur in regions containing small cancer lesions. Only cancer lesions with a minimum size of two voxels can be detected. Consequently, small lesions are hard to identify with metabolomic imaging, as some voxels partly cover the small cancerous lesion and benign tissue. The tumor might be missed. At last, metabolomic imaging is weaker in detecting cancer lesions on the edge of the prostate because the spectra of the edge voxels are partly distorted by magnetic susceptibility.

### **4.3.3 Comparison with histopathology**

The probably most important limitation of the present study was the comparison with histopathology. As histopathology currently is the gold standard in PCa diagnostics, this step



served as a tool to confirm the detection rate of the metabolomic MRSI method. Therefore, inaccuracies of this comparison do not affect the diagnostic technique itself, but potentially influence its detection rate.

Although a method to identify the histological slide approximate to the prostate center was developed and proven to be applicable, one significant problem remained: the identified "histological middle slides" most probably did not represent the identical planes that were scanned as "MRSI middle slices". No labeling of those MRSI middle slices was performed before the prostates were cut for histopathological evaluation. Consequently, some histological tumor lesions may have been missed by the metabolomic maps, because they did not occur on the MRSI cross-sectional plane, causing a (falsely) lowered detection rate. In order to prevent this potential error, maximum distances between a MRS-suspicious region and a corresponding histological tumor lesion of one direct or half a diagonal adjacent voxel were tolerated. However, because no significant differences between detected and undetected tumors were found (which could also be due to the small sample size), an imprecise alignment of MRSI and histological information might have occurred.

Furthermore, the alignment of histological slide and MRSI slice was performed manually. Therefore slight inaccuracies cannot be excluded.

In summary, a substantial limitation was that not exactly the same region has been analyzed by MRSI and the pathologist in the present study. It is expected that a precise marking of the center plane in future studies would result in a higher sensitivity rate of the metabolomic imaging technique.

#### **4.4 Conclusion and outlook**

The present study demonstrates the potential of metabolomic imaging as a diagnostic tool for PCa diagnostics. The cancer detection rate was however lower than expected. The strength of the concept to measure a whole dataset rather than single parameters was already proven in the fields of genomics and proteomics, and metabolomic strategies have already shown their clinical utility within brain cancer diagnostics<sup>106</sup>. Therefore, a transmission into prostate cancer diagnostics seems realistic. The lower detection rate within the present study (compared to our in-lab pilot study of 2005) may not result from the inclusion of the whole metabolome, but rather from difficulties in applying the technique to whole prostates.

In contrast to current PCa diagnostics, metabolomics are extremely cancer-specific. The metabolomic MRSI method of the present study however lacks a high specificity. Moreover, the high technical effort may prevent implementation as a screening tool. Metabolomic research on patients' blood sera might be more promising in this field.

Moreover, a clinical application of metabolomic imaging in PCa diagnostics is not easily possible at present. Assuming an adequate sensitivity, the next challenge will be the translation from an *ex vivo* to an *in vivo* (non-invasive) approach. The use of lower field strengths, such as 3T or 1.5T, needs to be considered, especially since 7T scanners currently are not available in many clinical facilities. However, a lower field strength would result in decreased spectral resolution and thus decreased sensitivity.

Another focus of future research in this field is to explain the lowered detection rate and to analyze benign prostatic hyperplasia and its influence on the metabolomic voxel values. Furthermore, the sensitivity to predict tumor aggressiveness needs to be evaluated by comparing two groups with low- and high-grade cancer. At the same time, a correlation of the MRSI outcome with pre-treatment PSA values might be useful, as the PSA is another known risk factor of PCa progression.

The technique of the present study might support a reliable prediction of tumor aggressiveness and thus prevent men with low-grade prostate from receiving highly invasive treatments. Metabolomic imaging may further be useful in surveillance of cancer growth in patients with asymptomatic PCa. Apart from this, it may indicate suspicious prostatic regions and guide biopsy, in order to avoid false negatives.

## 5. Summary

With an estimated 161,360 new cases in 2017 in the USA, PCa remains an epidemiologically important topic. However, the current diagnostic protocol remains insufficient, leading to overtreatment including side effects of therapy. A more reliable and highly cancer-specific diagnostic system is needed - preferably with an *in vivo* approach - that could allow for the detection of PCa lesions before biopsy and decrease the number of false positives at the same time. Furthermore, a radiological tool to guide biopsy and thus reduce false negatives and re-biopsies is necessary, as well as a reliable prediction of the malignant potential, before radical treatment is performed.

In a preliminary study, first steps in order to develop such a diagnostic tool by creating and analyzing metabolomic maps using MRS at 7T were made. In contrast to other studies, the spectral analysis included 36 metabolic regions rather than focusing on a small group of metabolites. Research showed that the inclusion of the whole measurable metabolome - referred to as "metabolomics" - gives a more complete depiction of metabolic alterations among cancer cells. The present study has been designed to further test the metabolomic PCa profile in a larger sample size as well as a partial automation of the process. In order to test the reliability of this system - also known as "metabolomic imaging" - the results were compared with histopathological findings as gold standard.

Thirty whole prostates with biopsy-proven PCa were analyzed with a 7T human MR scanner. The MR image as well as MR spectroscopy were recorded at the middle transverse cross-sectional plane for each specimen. Then, the image and the spectroscopy voxel grid were overlaid. After MRSI, the prostate samples were cut and analyzed with conventional histopathology.

Partial automation for spectral data processing was achieved using an in-house MATLAB-based program. MR spectra of all voxels were compared with the metabolomic PCa profile, that had been established within the preliminary study with a 14T spectrometer, to identify "MRS-suspicious regions". For each MRS-suspicious region, a "Malignancy Index" (MI) was calculated. MRSI center planes were overlaid and aligned with the histopathological results in order to compare the locations of the MRS-suspicious regions with the histologically identified cancer lesions.

Sixty-one percent of the histological cancer lesions were detected by metabolomic imaging. Among prostates with cancer on the examined middle slice, 75% were identified as cancerous. None of the analyzed parameters significantly differed between detected and undetected cancer lesions and there currently is no explanation for missed lesions. The MI could significantly differentiate between cancerous and benign MRS-suspicious regions ( $p = 0.006$ ) with an overall accuracy of 70%. Among detected tumor lesions, a significant positive correlation of MI and Gleason grade was shown ( $p = 0.021$ ). Thus, the MI serves as a marker of tumor aggressiveness. Moreover, malignant MRS-suspicious regions showed a tendency towards higher MI values corresponding with higher volumes of the detected tumor ( $p = 0.060$ ). Furthermore, a smaller Weighted Distance between the center of a three-dimensional histological tumor and the corresponding MRS-suspicious lesion resulted in higher MI values for this region ( $p = 0.000$ ).

In order to raise the cancer detection rate, an alternative analysis with a lower threshold for suspicious metabolomic voxel values was performed. This resulted in an elevated detection rate from 72% to 83%. However, the MI lost its power to significantly differentiate between malignant and benign MRS-suspicious regions. Thus, a higher sensitivity was reached, while the specificity decreased at the same time.

Recognizing its limitations, metabolomic imaging using MRSI is a non-invasive, highly PCa-specific diagnostic system that may be able to successfully address the current challenges in PCa diagnostics. However, further modifications need to be done, especially for an *in vivo* application. It is hoped that the present study may encourage further research in this field.

## Glossary

<b>Average Voxel Value (Avg)</b>	Average metabolomic voxel value per square millimeter, calculated for a MRS-suspicious region.
<b>(C+C)/C</b>	The metabolic ratio of (choline+creatine) over citrate is widely used within PCa research and showed its strong potential to detect prostate cancer. Due to specific alterations of those metabolites within prostate cancer cells, a ratio above 0.75 is considered as cancer-suspicious.
<b>correlation coefficient</b>	A statistical variable that measures the strength and direction of a linear relationship between two variables. It can be used to compare the strengths of correlations between different variables.
<b>detected and undetected cancer lesions</b>	Histologically identified cancer lesions that correspond with a MRS-suspicious lesions are referred to as "detected cancer lesions". In contrast, those histological cancer lesions that are missed by MRSI are called "undetected".
<b>effect size</b>	A statistical variable that measures the magnitude of a difference between two groups. It can be used to compare the strengths of different variables to distinguish two groups.
<b>Gleason grade</b>	Architectural pattern of a single prostate cancer lesion. Spans from 1 (very well differentiated) to 5 (very poorly differentiated) and is risk factor for tumor aggressiveness.
<b>Gleason score</b>	The sum of the most and second most prevalent Gleason grades within a prostate with histologically-proven PCa. Ranges from 2 to 10 and is a risk factor for tumor aggressiveness.
<b>histological cancer lesion</b>	A cancer lesions that was identified within the histopathological evaluation.
<b>histological middle slide</b>	The transverse histological slide that lies most closely to the middle slice of the prostate after cutting. In the present

study it could not be assured that the middle slice that was scanned with the MR spectrometer was identical with the histological middle slide.

<b>HRMAS <sup>1</sup>H MRS</b>	High resolution magic angle spinning proton magnetic resonance spectroscopy - a type of MR spectroscopy that had revolutionized the <i>ex vivo</i> research of PCa, as solid samples could be scanned with high resolution and without sacrificing the tissue architecture (allowing subsequent histopathological analysis).
<b>(<i>M+SD</i>)</b>	Empirical threshold of median plus one standard deviation regarding the metabolomic voxel values of one prostate MRS slice. Within the preliminary study, all histologically benign voxel values fell below this threshold. Therefore, ( <i>M+SD</i> ) was set as a border with metabolomic voxel values above indicating PCa. As this threshold was set arbitrarily, an alternative analysis with a lower threshold of ( <i>M+0.75SD</i> ) was performed.
<b>magnetic resonance imaging (MRI)</b>	A medical imaging technique based on nuclear magnetic resonance, providing an anatomical image.
<b>magnetic resonance spectroscopy (MRS)</b>	A technique based on nuclear magnetic resonance in order to measure biochemical alterations. It enables the identification as well as quantification of metabolites.
<b>magnetic resonance spectroscopy imaging (MRSI)</b>	A technique which combines MRI and MRS by overlaying the voxel grid with the spectral information obtained by MRS and the anatomical picture of the same slice acquired by MRI. By this, regions with metabolic alterations can be matched to the anatomical region.
<b>Malignancy Index (MI)</b>	The MI sums up the total elevation of the metabolomic voxel values of a MRS-suspicious region.
<b>MATLAB</b>	A software environment commonly used by scientists and engineers. Within the present study, two MATLAB-based programs, both developed by the engineer Yannick Berker, were used: a) for a partly automation of the spectral processing and analysis; b) to build a 3D dataset

of the histological slides for a calculation of tumor volumes and distances between specific points.

---

<b>metabolomic field effect</b>	The metabolomic field effect means cancer-specific metabolic changes among non-neoplastic cells in prostates with PCa. This phenomenon was observed within in-lab research (unpublished data, manuscript in review).
<b>metabolomic imaging</b>	Creation of metabolomic maps using MRSI and including the spectral information of the whole metabolome, rather than single metabolites (referred to as "metabolic imaging").
<b>metabolomic PCa profile</b>	A PCa-specific profile including the spectral changes within 36 metabolite regions in cancer cells, that was obtained by previous analyses on the intact tissue 14T HRMAS <sup>1</sup> H MR spectrometer <sup>84,104</sup> . This profile can be compared with any other prostate spectrum in order to identify potentially cancerous regions.
<b>metabolomic voxel value</b>	A voxel receives a metabolomic value during the process of Profile Fitting, when the spectrum of the voxel is compared with the applied metabolomic cancer profile. A spectrum similar to the metabolomic profile results in a higher metabolomic voxel value with higher possibility for cancer. A "smoothed" metabolomic voxel value is obtained after a convolution process including the values of the surrounding voxels, in order to average out noise influences.
<b>MRS-suspicious region</b>	A region of minimum two directly adjacent voxels with cancer-suspicious metabolomic values (above the threshold ( $M+SD$ )). A MRS-suspicious region is labeled as "malignant", if it corresponds with (and thus detects) a histological cancer lesion. Otherwise, it is referred to as "benign" or "false positive".
<b>overall loading factors</b>	Parameters of the metabolomic PCa profile. Each factor is matched to a certain metabolic region. The more a certain metabolic region contributes to the cancer profile, the

---

higher the loading factor.

---

**Preliminary study**

In the present study, "preliminary study" means an in-house study published in 2010<sup>104</sup>. Here, the prostate cancer profile for the metabolomic imaging was first tested on five whole prostates. The present study was designed to improve and further test this technique.

---

**Profile Fitting**

A (within the present study) automated process, in which the metabolomic PCa profile is applied to a voxel grid in order to obtain a metabolomic map of this slice.

---

**Weighted Distance**

The range between the 3D histological tumor center to the corresponding MRS-suspicious region's middle point, normalized by the number of voxels of this MRS region.



## List of Figures

<b>Figure 1</b>	Screenshot of 7T scan .....	<b>15</b>
<b>Figure 2</b>	Definition of the MRS region of interest in MATLAB .....	<b>17</b>
<b>Figure 3</b>	Voxel spectrum after automatic preprocessing .....	<b>17</b>
<b>Figure 4</b>	Voxel spectrum after manual correction.....	<b>18</b>
<b>Figure 5</b>	Metabolomic cancer map after Profile Fitting.....	<b>20</b>
<b>Figure 6</b>	Identification of MRS-suspicious regions among the MATLAB-export of the voxel values.....	<b>21</b>
<b>Figure 7</b>	Standardized picture of a histological slide .....	<b>23</b>
<b>Figure 8</b>	MRI slice surface area calculation with OsiriX.....	<b>25</b>
<b>Figure 9</b>	Identification of anterior/posterior: the urethra's shape .....	<b>26</b>
<b>Figure 10</b>	Identification of anterior/posterior: position of the seminal vesicles.....	<b>27</b>
<b>Figure 11</b>	Adaption of the voxel grid .....	<b>28</b>
<b>Figure 12</b>	Adaption of the histological slide .....	<b>29</b>
<b>Figure 13</b>	Comparison between MRS-suspicious lesion and histological tumor region in the same voxel grid .....	<b>29</b>
<b>Figure 14</b>	Distances of interest .....	<b>31</b>
<b>Figure 15</b>	Graph of the average volume percentages of all seven- and eight-slide cases ...	<b>35</b>
<b>Figure 16</b>	Identification of the histological middle slide - case 2 .....	<b>35</b>
<b>Figure 17</b>	Comparison of MRI average slice surface areas and average histological slide volume percentages.....	<b>36</b>
<b>Figure 18</b>	ROC curve of the MI .....	<b>37</b>
<b>Figure 19</b>	Differentiation of metabolomic voxel values between samples of malignant and benign pathology.....	<b>71</b>
<b>Figure 20</b>	Cancer detection using the MI .....	<b>71</b>
<b>Figure 21</b>	Comparison of the average voxel intensity and Weighted Distance .....	<b>72</b>
<b>Figure 22</b>	Possible effect of a lowered threshold .....	<b>72</b>
<b>Figure 23</b>	Prostate anatomy.....	<b>73</b>

## List of Tables

<b>Table 1</b>	Patient population .....	<b>14</b>
<b>Table 2</b>	Convolution matrix for smoothing of voxel cancer values in order to reduce noise effects.....	<b>19</b>
<b>Table 3</b>	Cases without a histological tumor lesion on the middle slide.....	<b>39</b>
<b>Table 4</b>	List of the overall loading factors .....	<b>74</b>
<b>Table 5</b>	Coordinates of the Malignancy Index ROC curve.....	<b>76</b>

## References

- 1 Torre LA, Bray F, Siegel RL, Ferlay J, Lortet-Tieulent J, Jemal A. Global cancer statistics, 2012. *CA: A Cancer Journal for Clinicians* 2015;65: 87–108.
- 2 Siegel RL, Miller KD, Jemal A. Cancer Statistics, 2017. *CA: A Cancer Journal for Clinicians* 2017;67: 7–30.
- 3 Miller KD, Siegel RL, Lin CC, Mariotto AB, Kramer JL, Rowland JH, et al. Cancer treatment and survivorship statistics, 2016. *CA: A Cancer Journal for Clinicians* 2016;66: 271–89.
- 4 Stephenson AJ, Kattan MW, Eastham JA, Bianco FJ, Yossepowitch O, Vickers AJ, et al. Prostate Cancer-Specific Mortality After Radical Prostatectomy for Patients Treated in the Prostate-Specific Antigen Era. *Journal of Clinical Oncology* 2009;27: 4300–5.
- 5 DeSantis CE, Lin CC, Mariotto AB, Siegel RL, Stein KD, Kramer JL, et al. Cancer treatment and survivorship statistics, 2014. *CA A Cancer Journal for Clinicians* 2014;64: 252–71.
- 6 American Cancer Society. Cancer Facts & Figures 2017. *American Cancer Society, Atlanta* 2017.
- 7 Center MM, Jemal A, Lortet-Tieulent J, Ward E, Ferlay J, Brawley O, et al. International Variation in Prostate Cancer Incidence and Mortality Rates. *European Urology* 2012;61: 1079–92.
- 8 American Cancer Society. Prostate Cancer Prevention and Early Detection. *Cancer Information Database* 2014.
- 9 American Urological Association. Early Detection of Prostate Cancer: AUA Guideline 2013.
- 10 Sandblom G, Varenhorst E, Rosell J, Löfman O, Carlsson P. Randomised prostate cancer screening trial: 20 year follow-up. *BMJ* 2011;342: d1539.
- 11 World Health Organization Classification of Tumours. Pathology and Genetics of Tumours of the Urinary System and Male Genital Organs. *IARC Press, Lyon* 2004.
- 12 American Urological Association. PSA Testing for the Pretreatment Staging and Posttreatment management of Prostate Cancer: 2013 Revision of 2009 Best Practice Statement 2013.
- 13 Mistry K, Cable G. Meta-Analysis of Prostate-Specific Antigen and Digital Rectal Examination as Screening Tests for Prostate Carcinoma. *The Journal of the American Board of Family Medicine* 2003;16: 95–101.

- 14 U.S. Preventive Services Task Force. Draft Recommendation Statement: Prostate Cancer: Screening - US Preventive Services Task Force.  
*<https://www.uspreventiveservicestaskforce.org/Page/Document/draft-recommendation-statement/prostate-cancer-screening1> (accessed 29 Nov 2017).*
- 15 Eichler K, Hempel S, Wilby J, Myers L, Bachmann LM, Kleijnen J. Diagnostic Value of Systematic Biopsy Methods in the Investigation of Prostate Cancer: A Systematic Review. *The Journal of Urology* 2006;175: 1605–12.
- 16 Epstein JI, Allsbrook WC, Amin MB, Egevad LL. The 2005 International Society of Urological Pathology (ISUP) Consensus Conference on Gleason Grading of Prostatic Carcinoma. *Am. J. Surg. Pathol.* 2005;29: 1228–42.
- 17 Pisansky TM, Kahn MJ, Rasp GM, Cha SS, Haddock MG, Bostwick DG. A multiple prognostic index predictive of disease outcome after irradiation for clinically localized prostate carcinoma. *Cancer* 1997;79: 337–44.
- 18 Hull G, Rabbani F, Abbas F, Wheeler T, Kattan M, Scardino P. Cancer Control With Radical Prostatectomy alone in 1,000 Consecutive Patients. *The Journal of Urology* 2002;167: 528–34.
- 19 Partin AW, Yoo J, Carter HB, Pearson JD, Chan DW, Epstein JI, et al. The use of prostate specific antigen, clinical stage and Gleason score to predict pathological stage in men with localized prostate cancer. *The Journal of Urology* 1993;150: 110–4.
- 20 Steyerberg EW, Roobol MJ, Kattan MW, van der Kwast, T H, de Koning, H J, Schröder FH. Prediction of indolent prostate cancer: validation and updating of a prognostic nomogram. *The Journal of Urology* 2007;177: 107-12; discussion 112.
- 21 Shariat SF, Karakiewicz PI, Margulis V, Kattan MW. Inventory of prostate cancer predictive tools. *Current Opinion in Urology* 2008;18: 279–96.
- 22 Graefen M, Haese A, Pichlmeier U, Hammerer PG, Noldus J, Butz K, et al. A validated strategy for side specific prediction of organ confined prostate cancer: a tool to select for nerve sparing radical prostatectomy. *The Journal of Urology* 2001;165: 857–63.
- 23 Augustin H, Eggert T, Wenske S, Karakiewicz PI, Palisaar J, Daghofer F, et al. Comparison of accuracy between the Partin tables of 1997 and 2001 to predict final pathological stage in clinically localized prostate cancer. *The Journal of Urology* 2004;171: 177–81.
- 24 Ohori M, Kattan MW, Koh H, Maru N, Slawin KM, Shariat S, et al. Predicting the presence and side of extracapsular extension: a nomogram for staging prostate cancer. *The Journal of Urology* 2004;171: 1844-9; discussion 1849.

- 25 Ahmed HU, Emberton M. The role of magnetic resonance imaging in targeting prostate cancer in patients with previous negative biopsies and elevated prostate-specific antigen levels. *BJU Int.* 2009;104: 269-70; author reply 270.
- 26 Cheikh AB, Girouin N, Colombel M, Maréchal J-M, Gelet A, Bissery A, et al. Evaluation of T2-weighted and dynamic contrast-enhanced MRI in localizing prostate cancer before repeat biopsy. *Eur Radiol* 2009;19: 770–8.
- 27 Lawrentschuk N, Fleshner N. The role of magnetic resonance imaging in targeting prostate cancer in patients with previous negative biopsies and elevated prostate-specific antigen levels. *BJU international* 2009;103: 730–3.
- 28 Labanaris AP, Engelhard K, Zugor V, Nutzler R, Kuhn R. Prostate cancer detection using an extended prostate biopsy schema in combination with additional targeted cores from suspicious images in conventional and functional endorectal magnetic resonance imaging of the prostate. *Prostate cancer and prostatic diseases* 2010;13: 65–70.
- 29 Lindenberg L, Ahlman M, Turkbey B, Mena E, Choyke P. Advancement of MR and PET/MR in Prostate Cancer. *Seminars in nuclear medicine* 2016;46: 536–43.
- 30 Sweat SD, Pacelli A, Murphy GP, Bostwick DG. Prostate-specific membrane antigen expression is greatest in prostate adenocarcinoma and lymph node metastases. *Urology* 1998;52: 637–40.
- 31 Rowe SP, Gorin MA, Allaf ME, Pienta KJ, Tran PT, Pomper MG, et al. PET imaging of prostate-specific membrane antigen in prostate cancer: current state of the art and future challenges. *Prostate cancer and prostatic diseases* 2016;19: 223–30.
- 32 Holland JP, Divilov V, Bander NH, Smith-Jones PM, Larson SM, Lewis JS. 89Zr-DFO-J591 for immunoPET of prostate-specific membrane antigen expression in vivo. *Journal of nuclear medicine : official publication, Society of Nuclear Medicine* 2010;51: 1293–300.
- 33 Afshar-Oromieh A, Avtzi E, Giesel FL, Holland-Letz T, Linhart HG, Eder M, et al. The diagnostic value of PET/CT imaging with the (68)Ga-labelled PSMA ligand HBED-CC in the diagnosis of recurrent prostate cancer. *European journal of nuclear medicine and molecular imaging* 2015;42: 197–209.
- 34 Eiber M, Maurer T, Souvatzoglou M, Beer AJ, Ruffani A, Haller B, et al. Evaluation of Hybrid (6)(8)Ga-PSMA Ligand PET/CT in 248 Patients with Biochemical Recurrence After Radical Prostatectomy. *Journal of nuclear medicine : official publication, Society of Nuclear Medicine* 2015;56: 668–74.

- 35 Ross JS, Sheehan CE, Fisher HAG, Kaufman RP, JR, Kaur P, Gray K, et al. Correlation of primary tumor prostate-specific membrane antigen expression with disease recurrence in prostate cancer. *Clinical cancer research : an official journal of the American Association for Cancer Research* 2003;9: 6357–62.
- 36 Perner S, Hofer MD, Kim R, Shah RB, Li H, Moller P, et al. Prostate-specific membrane antigen expression as a predictor of prostate cancer progression. *Human pathology* 2007;38: 696–701.
- 37 Osborne JR, Green DA, Spratt DE, Lyashchenko S, Fareedy SB, Robinson BD, et al. A prospective pilot study of (89)Zr-J591/prostate specific membrane antigen positron emission tomography in men with localized prostate cancer undergoing radical prostatectomy. *The Journal of Urology* 2014;191: 1439–45.
- 38 Rowe SP, Gage KL, Faraj SF, Macura KJ, Cornish TC, Gonzalez-Roibon N, et al. (1)(8)F-DCFBC PET/CT for PSMA-Based Detection and Characterization of Primary Prostate Cancer. *Journal of nuclear medicine : official publication, Society of Nuclear Medicine* 2015;56: 1003–10.
- 39 Schröder Fritz H., Hugosson Jonas, Roobol Monique J., Tammela Teuvo L.J., Ciatto Stefano, Nelen Vera, Kwiatkowski Maciej, Lujan Marcos, Lilja Hans, Zappa Marco, Denis Louis J., Recker Franz, Berenguer Antonio, Määttänen Liisa, Bangma Chris H., Aus Gunnar, Villers Arnauld, Rebillard Xavier, van der Kwast Theodorus, Blijenberg Bert G., Moss Sue M., de Koning Harry J., Auvinen Anssi. Screening and Prostate-Cancer Mortality in a Randomized European Study. *The New England Journal of Medicine* 2009;360: 1320–8.
- 40 Rosario DJ, Lane JA, Metcalfe C, Donovan JL, Doble A, Goodwin L, et al. Short term outcomes of prostate biopsy in men tested for cancer by prostate specific antigen: prospective evaluation within ProtecT study. *BMJ (Clinical research ed.)* 2012;344: d7894.
- 41 Katz DA, Jarrard DF, McHorney CA, Hillis SL, Wiebe DA, Fryback DG. Health Perceptions in Patients Who Undergo Screening and Workup for Prostate Cancer. *Urology* 2007;69: 215–20.
- 42 Schröder FH, Hugosson J, Roobol MJ, Tammela, Teuvo L J, Ciatto S, Nelen V, et al. Prostate-cancer mortality at 11 years of follow-up. *The New England Journal of Medicine* 2012;366: 981–90.
- 43 Andriole GL, Crawford ED, Grubb RL, Buys SS, Chia D, Church TR, et al. Prostate Cancer Screening in the Randomized Prostate, Lung, Colorectal, and Ovarian Cancer

- Screening Trial: Mortality Results after 13 Years of Follow-up. *JNCI Journal of the National Cancer Institute* 2012;104: 125–32.
- 44 Shoag JE, Mittal S, Hu JC. Reevaluating PSA Testing Rates in the PLCO Trial. *The New England Journal of Medicine* 2016;374: 1795–6.
- 45 Tsodikov A, Gulati R, Heijnsdijk EAM, Pinsky PF, Moss SM, Qiu S, et al. Reconciling the Effects of Screening on Prostate Cancer Mortality in the ERSPC and PLCO Trials. *Annals of Internal Medicine* 2017;167: 449–55.
- 46 Visschere P de, Oosterlinck W, Meerleer G de, Villeirs G. Clinical and imaging tools in the early diagnosis of prostate cancer, a review. *JBR-BTR : organe de la Société royale belge de radiologie (SRBR) = orgaan van de Koninklijke Belgische Vereniging voor Radiologie (KBVR)* 2010;93: 62–70.
- 47 Ploussard G, Nicolaiew N, Marchand C, Terry S, Allory Y, Vacherot F, et al. Risk of repeat biopsy and prostate cancer detection after an initial extended negative biopsy: longitudinal follow-up from a prospective trial. *BJU Int* 2013;111: 988–96.
- 48 Lee HY, Lee HJ, Byun S-S, Lee SE, Hong SK, Kim SH. Classification of Focal Prostatic Lesions on Transrectal Ultrasound (TRUS) and the Accuracy of TRUS to Diagnose Prostate Cancer. *Korean J Radiol* 2009;10: 244.
- 49 Campos-Fernandes J-L, Bastien L, Nicolaiew N, Robert G, Terry S, Vacherot F, et al. Prostate Cancer Detection Rate in Patients with Repeated Extended 21-Sample Needle Biopsy. *European Urology* 2009;55: 600–9.
- 50 Scattoni V, Raber M, Capitanio U, Abdollah F, Roscigno M, Angiolilli D, et al. The Optimal Rebiopsy Prostatic Scheme Depends on Patient Clinical Characteristics: Results of a Recursive Partitioning Analysis Based on a 24-Core Systematic Scheme. *European Urology* 2011;60: 834–41.
- 51 Hansen NL, Kesch C, Barrett T, Koo B, Radtke JP, Bonekamp D, et al. Multicentre evaluation of target and systematic biopsies using Magnetic Resonance and Ultrasound Image-Fusion guided Transperineal Prostate Biopsy in patients with a previous negative biopsy. *BJU international* 2016.
- 52 Sciarra A, Panebianco V, Ciccariello M, Salciccia S, Cattarino S, Lisi D, et al. Value of magnetic resonance spectroscopy imaging and dynamic contrast-enhanced imaging for detecting prostate cancer foci in men with prior negative biopsy. *Clinical cancer research : an official journal of the American Association for Cancer Research* 2010;16: 1875–83.

- 53 Daskivich TJ, Chamie K, Kwan L, Labo J, Palvolgyi R, Dash A, et al. Overtreatment of men with low-risk prostate cancer and significant comorbidity. *Cancer* 2011;117: 2058–66.
- 54 Potosky Arnold L., Legler J, Albertsen PC, Stanford JL, Gilliland FD, Hamilton AS, et al. Health Outcomes After Prostatectomy or Radiotherapy for Prostate Cancer: Results From the Prostate Cancer Outcomes Study. *Journal of the National Cancer Institute* 2000;Vol. 92, No. 19: 1582–92.
- 55 Tuppin P, Samson S, Fagot-Campagna A, Lukacs B, Alla F, Paccaud F, et al. Prostate cancer outcomes in France: treatments, adverse effects and two-year mortality. *BMC Urol* 2014;14: 48.
- 56 Carlsson S, Drevin L, Loeb S, Widmark A, Lissbrant IF, Robinson D, et al. Population-based study of long-term functional outcomes after prostate cancer treatment. *BJU Int* 2015: n/a.
- 57 Barocas DA, Cowan JE, Smith JA, Carroll PR. What Percentage of Patients With Newly Diagnosed Carcinoma of the Prostate are Candidates for Surveillance? An Analysis of the CaPSURE™ Database. *The Journal of Urology* 2008;180: 1330–5.
- 58 Cooperberg MR, Broering JM, Carroll PR. Time Trends and Local Variation in Primary Treatment of Localized Prostate Cancer. *Journal of Clinical Oncology* 2010;28: 1117–23.
- 59 Thapar R, Titus M. Recent Advances in Metabolic Profiling and Imaging of Prostate Cancer. *CMB* 2014;2: 53–69.
- 60 DeFeo EM, Wu C-L, McDougal WS, Cheng LL. A decade in prostate cancer: from NMR to metabolomics. *Nat Rev Urol* 2011;8: 301–11.
- 61 Spur E-M, Decelle EA, Cheng LL. Metabolomic imaging of prostate cancer with magnetic resonance spectroscopy and mass spectrometry. *Eur J Nucl Med Mol Imaging* 2013;40: 60–71.
- 62 Thapar R, Titus M. Recent Advances in Metabolic Profiling and Imaging of Prostate Cancer. *CMB* 2014;2: 53–69.
- 63 Swanson MG, Zektzer AS, Tabatabai ZL, Simko J, Jarso S, Keshari KR, et al. Quantitative analysis of prostate metabolites using <sup>1</sup>H HR-MAS spectroscopy. *Magn. Reson. Med.* 2006;55: 1257–64.
- 64 Schiebler ML, Miyamoto KK, White M, Maygarden SJ, Mohler JL. In vitro high resolution <sup>1</sup>H-spectroscopy of the human prostate: benign prostatic hyperplasia, normal peripheral zone and adenocarcinoma. - PubMed - NCBI 1993 Mar: 285–91.



- 65 Glunde K, Jacobs MA, Bhujwala ZM. Choline metabolism in cancer: implications for diagnosis and therapy. *Expert review of molecular diagnostics* 2006;6: 821–9.
- 66 Costello LC, Franklin RB. Concepts of citrate production and secretion by prostate. 1. Metabolic relationships. *The Prostate* 1991;18: 25–46.
- 67 Costello LC, Franklin RB. Bioenergetic theory of prostate malignancy. *The Prostate* 1994;25: 162–6.
- 68 Franklin RB, Costello LC. Intermediary energy metabolism of normal and malignant prostate epithelial cells. *Prostate: Basic and Clinical aspects. New York: CRC Press* 1997: 115–50.
- 69 Smith TA, Eccles S, Ormerod MG, Tombs AJ, Titley JC, Leach MO. The phosphocholine and glycerophosphocholine content of an oestrogen-sensitive rat mammary tumour correlates strongly with growth rate. *British journal of cancer* 1991;64: 821–6.
- 70 Milkevitch M, Shim H, Pilatus U, Pickup S, Wehrle JP, Samid D, et al. Increases in NMR-visible lipid and glycerophosphocholine during phenylbutyrate-induced apoptosis in human prostate cancer cells. *Biochimica et biophysica acta* 2005;1734: 1–12.
- 71 Glunde K, Serkova NJ. Therapeutic targets and biomarkers identified in cancer choline phospholipid metabolism. *Pharmacogenomics* 2006;7: 1109–23.
- 72 Jordan KW, Cheng LL. NMR-based metabolomics approach to target biomarkers for human prostate cancer. *Expert Review of Proteomics* 2007;4: 389–400.
- 73 Cheng LL, Wu C, Smith MR, Gonzalez RG. Non-destructive quantitation of spermine in human prostate tissue samples using HRMAS 1H NMR spectroscopy at 9.4 T. *FEBS letters* 2001;494: 112–6.
- 74 Stenman K, Stattin P, Stenlund H, Riklund K, Gröbner G, Bergh A. H HRMAS NMR Derived Bio-markers Related to Tumor Grade, Tumor Cell Fraction, and Cell Proliferation in Prostate Tissue Samples. *Biomarker insights* 2011;6: 39–47.
- 75 Cheng LL, Ma MJ, Becerra L, Ptak T, Tracey I, Lackner A, et al. Quantitative neuropathology by high resolution magic angle spinning proton magnetic resonance spectroscopy. *Proceedings of the National Academy of Sciences of the United States of America* 1997;94: 6408–13.
- 76 Cheng LL, Anthony DC, Comite AR, Black PM, Tzika AA, Gonzalez RG. Quantification of microheterogeneity in glioblastoma multiforme with ex vivo high-resolution magic-angle spinning (HRMAS) proton magnetic resonance spectroscopy. *Neuro-oncology* 2000;2: 87–95.

- 77 ANDREW ER, BRADBURY A, EADES RG. Removal of Dipolar Broadening of Nuclear Magnetic Resonance Spectra of Solids by Specimen Rotation. *Nature* 1959;183: 1802–3.
- 78 Cheng LL, Lean CL, Bogdanova A, Wright SC, Ackerman JL, Brady TJ, et al. Enhanced resolution of proton NMR spectra of malignant lymph nodes using magic-angle spinning. *Magnetic resonance in medicine* 1996;36: 653–8.
- 79 Cheng LL, Chang IW, Louis DN, Gonzalez RG. Correlation of high-resolution magic angle spinning proton magnetic resonance spectroscopy with histopathology of intact human brain tumor specimens. *Cancer research* 1998;58: 1825–32.
- 80 Taylor JL, Wu C-L, Cory D, Gonzalez RG, Bielecki A, Cheng LL. High-resolution magic angle spinning proton NMR analysis of human prostate tissue with slow spinning rates. *Magnetic resonance in medicine* 2003;50: 627–32.
- 81 Swanson MG, Keshari KR, Tabatabai ZL, Simko JP, Shinohara K, Carroll PR, et al. Quantification of choline- and ethanolamine-containing metabolites in human prostate tissues using <sup>1</sup>H HR-MAS total correlation spectroscopy. *Magnetic resonance in medicine* 2008;60: 33–40.
- 82 Tomlins AM, Foxall PJD, Lindon JC, Nicholson JK, Lynch MJ, Spraul M, et al. High resolution magic angle spinning <sup>1</sup>H nuclear magnetic resonance analysis of intact prostatic hyperplastic and tumour tissues. *Analytical Communications* 1998: 113–5.
- 83 Ratiney H, Albers MJ, Rabeson H, Kurhanewicz J. Semi-parametric time-domain quantification of HR-MAS data from prostate tissue. *NMR in biomedicine* 2010;23: 1146–57.
- 84 Cheng LL, Burns MA, Taylor JL, He W, Halpern EF, McDougal WS, et al. Metabolic characterization of human prostate cancer with tissue magnetic resonance spectroscopy. *Cancer research* 2005;65: 3030–4.
- 85 Fuss T, Cheng L. Evaluation of Cancer Metabolomics Using ex vivo High Resolution Magic Angle Spinning (HRMAS) Magnetic Resonance Spectroscopy (MRS). *Metabolites* 2016;6: 11.
- 86 Scheidler J, Hricak H, Vigneron DB, Yu KK, Sokolov DL, Huang LR, et al. Prostate cancer: localization with three-dimensional proton MR spectroscopic imaging--clinicopathologic study. *Radiology* 1999;213: 473–80.
- 87 Maxeiner A, Adkins CB, Zhang Y, Taupitz M, Halpern EF, McDougal WS, et al. Retrospective analysis of prostate cancer recurrence potential with tissue metabolomic profiles. *Prostate* 2009: n/a.

- 88 Swanson MG, Vigneron DB, Tabatabai ZL, Males RG, Schmitt L, Carroll PR, et al. Proton HR-MAS spectroscopy and quantitative pathologic analysis of MRI/3D-MRSI-targeted postsurgical prostate tissues. *Magn. Reson. Med.* 2003;50: 944–54.
- 89 Mueller-Lisse UG, Swanson MG, Vigneron DB, Hricak H, Bessette A, Males RG, et al. Time-dependent effects of hormone-deprivation therapy on prostate metabolism as detected by combined magnetic resonance imaging and 3D magnetic resonance spectroscopic imaging. *Magnetic resonance in medicine* 2001;46: 49–57.
- 90 Yuen JSP, Thng CH, Tan PH, Khin LW, Phee SJL, Xiao D, et al. Endorectal magnetic resonance imaging and spectroscopy for the detection of tumor foci in men with prior negative transrectal ultrasound prostate biopsy. *The Journal of Urology* 2004;171: 1482–6.
- 91 Nagarajan R, Margolis D, Raman S, Sarma MK, Sheng K, King CR, et al. MR spectroscopic imaging and diffusion-weighted imaging of prostate cancer with Gleason scores. *Journal of magnetic resonance imaging : JMRI* 2012;36: 697–703.
- 92 Prando A, Kurhanewicz J, Borges AP, Oliveira EM, Figueiredo E. Prostatic biopsy directed with endorectal MR spectroscopic imaging findings in patients with elevated prostate specific antigen levels and prior negative biopsy findings: early experience. *Radiology* 2005;236: 903–10.
- 93 Mueller-Lisse UG, Scherr MK. Proton MR spectroscopy of the prostate. *European Journal of Radiology* 2007;63: 351–60.
- 94 Kurhanewicz J, Vigneron DB, Hricak H, Narayan P, Carroll P, Nelson SJ. Three-dimensional H-1 MR spectroscopic imaging of the in situ human prostate with high (0.24-0.7-cm<sup>3</sup>) spatial resolution. *Radiology* 1996;198: 795–805.
- 95 Wang P, Guo Y-m, Liu M, Qiang Y-q, Guo X-j, Zhang Y-l, et al. A Meta-Analysis of the Accuracy of Prostate Cancer Studies Which Use Magnetic Resonance Spectroscopy as a Diagnostic Tool. *Korean J Radiol* 2008;9: 432.
- 96 Mueller-Lisse UG, Vigneron DB, Hricak H, Swanson MG, Carroll PR, Bessette A, et al. Localized prostate cancer: effect of hormone deprivation therapy measured by using combined three-dimensional 1H MR spectroscopy and MR imaging: clinicopathologic case-controlled study. *Radiology* 2001;221: 380–90.
- 97 Jung JA, Coakley FV, Vigneron DB, Swanson MG, Qayyum A, Weinberg V, et al. Prostate depiction at endorectal MR spectroscopic imaging: investigation of a standardized evaluation system. *Radiology* 2004;233: 701–8.

- 98 Wefer AE, Hricak H, Vigneron DB, Coakley FV, Lu Y, Wefer J, et al. Sextant localization of prostate cancer: Comparison of sextant biopsy, magnetic resonance imaging and magnetic resonance spectroscopic imaging with step section histology. *The Journal of Urology* 2000;164: 400–4.
- 99 Yu KK, Scheidler J, Hricak H, Vigneron DB, Zaloudek CJ, Males RG, et al. Prostate cancer: prediction of extracapsular extension with endorectal MR imaging and three-dimensional proton MR spectroscopic imaging. *Radiology* 1999;213: 481–8.
- 100 Zakian KL, Sircar K, Hricak H, Chen H-N, Shukla-Dave A, Eberhardt S, et al. Correlation of Proton MR Spectroscopic Imaging with Gleason Score Based on Step-Section Pathologic Analysis after Radical Prostatectomy<sup>1</sup>. *Radiology* 2005;234: 804–14.
- 101 Trock BJ. Application of metabolomics to prostate cancer. *Urologic Oncology: Seminars and Original Investigations* 2011;29: 572–81.
- 102 Sreekumar A, Poisson LM, Rajendiran TM, Khan AP, Cao Q, Yu J, et al. Metabolomic profiles delineate potential role for sarcosine in prostate cancer progression. *Nature* 2009;457: 910–4.
- 103 Griffin JL, Shockcor JP. Metabolic profiles of cancer cells. *Nature reviews. Cancer* 2004;4: 551–61.
- 104 Wu C-L, Jordan KW, Ratai EM, Sheng J, Adkins CB, DeFeo EM, et al. Metabolomic Imaging for Human Prostate Cancer Detection. *Science Translational Medicine* 2010;2: 16ra8.
- 105 Spratlin JL, Serkova NJ, Eckhardt SG. Clinical applications of metabolomics in oncology: a review. *Clinical cancer research : an official journal of the American Association for Cancer Research* 2009;15: 431–40.
- 106 Cheng LL, Pohl U, eds. *The role of NMR-based metabolomics in cancer*. Amsterdam: Elsevier, 2007; 345-74.
- 107 Berker Y. *Automation Of Metabolomic Imaging Procedure Based On Intact Tissue NMR Spectroscopy*. Aachen, 2010.
- 108 Kumar D, Gupta A, Mandhani A, Sankhwar SN. Metabolomics-Derived Prostate Cancer Biomarkers: Fact or Fiction? *J. Proteome Res.* 2015;14: 1455–64.
- 109 Giskeødegård GF, Hansen AF, Bertilsson H, Gonzalez SV, Kristiansen KA, Bruheim P, et al. Metabolic markers in blood can separate prostate cancer from benign prostatic hyperplasia. *Br J Cancer* 2015;113: 1712–9.

- 110 Kumar D, Gupta A, Mandhani A, Sankhwar SN. NMR spectroscopy of filtered serum of prostate cancer: A new frontier in metabolomics. *Prostate* 2016;76: 1106–19.
- 111 Ringnér M. What is principal component analysis? *Nat Biotechnol* 2008;26: 303–4.

## Appendices

### Construction of the metabolomic PCa profile

The translation of the measured metabolite intensities into a PCa-specific metabolomic profile was a great challenge owing to the complex metabolomic data matrix. As metabolomic techniques generate enormous amounts of data, a statistical method was necessary in order to manage the data without losing crucial information. Therefore the principal components analysis (PCA) became a popular technique within metabolomic research<sup>72</sup>. PCA is a common data reduction technique to identify patterns in big data sets without losing too much information during the process of data compression<sup>111</sup>. It defines independent principal components (PCs), which represent linear combinations of the measured metabolites with individual loading factors. The more a certain metabolite contributes to the cancer profile, the higher is the loading factor. Only a few of those principal components cover the major information of the entire metabolomic data matrix<sup>104,111</sup>.

In the pilot study of 2005, PCA was carried out on 36 metabolite regions containing the most relevant metabolites<sup>84</sup>. The previously established PCa-specific, concentration-based principal components had to be re-analyzed to ensure the applicability for different MR spectra of various prostate samples. Hence, the intensity of each of the 36 metabolite regions was normalized by the intensity of the total measured region (0.5-4.5 ppm). After the re-analysis, a new metabolomic PCa profile was calculated by selecting the most significant principal components. Using canonical analysis, individual coefficients for those four principal components were identified; thus the linear combination of the principal components could create a metabolomic profile which best characterized PCa cells and therefore significantly differentiated between malignant and benign prostatic tissue. Finally, the loading factors and canonical coefficients were combined to one variable, referred to as "overall loading factors"<sup>104</sup>.

In order to compare a random MR spectrum of a prostatic sample with this cancer profile, the spectrum's intensities of the 36 metabolite regions are combined with the overall loading factors for each region. This results in a metabolomic profile value that quantifies the correlation of the spectrum with the metabolomic profile, reflecting the potential (or suspicion) for cancer in this spectrum.

Figures

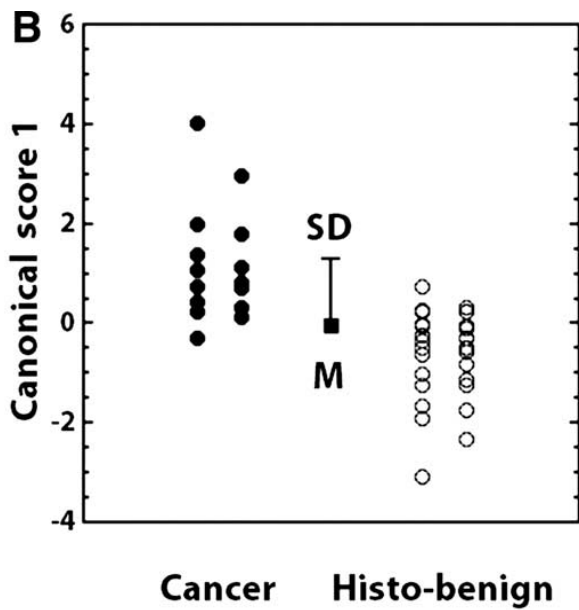


**Figure 19 Differentiation of metabolomic voxel values between samples of malignant and benign pathology.** Based on the metabolomic profile values (y-axis) of the 42 tested prostatic samples, a statistically significant differentiation between malignant (solid dots) and benign samples (open dots) was possible. The profile values of all benign samples fell under the empirical threshold of median (M) plus one standard deviation (SD). M and SD values were determined of all 42 samples.<sup>104</sup>

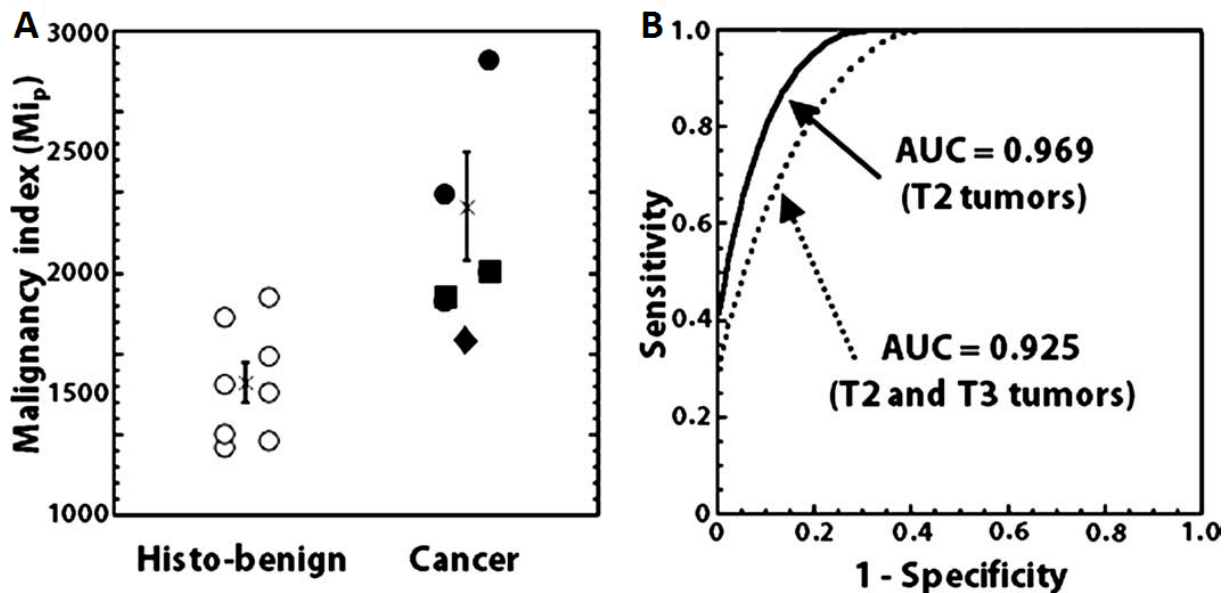


**Figure 20 Cancer detection using the MI.** **A:** The Malignancy Index (MI) significantly differentiates between MRS-suspicious lesions that truly correspond with a histologically proven cancer lesion ("Cancer", solid dots) from MRS-suspicious lesions that are considered as histologically benign ("Histo-benign", open dots) as they show elevated metabolomic profile values without a histological equivalent. **B:** The area under the curve (AUC) values of the MI indicate a high diagnostic accuracy of 93% for all tumors and of 97% for the pT2 tumors.<sup>104</sup>

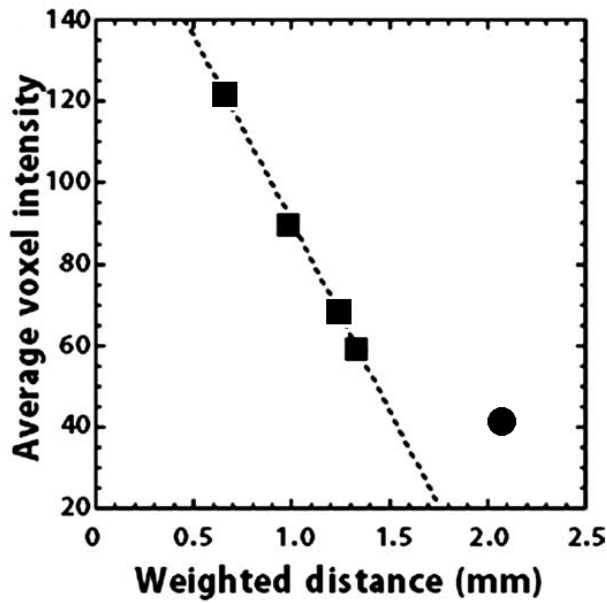


**Figure 21 Comparison of the average voxel intensity and Weighted Distance.** Among pT2 cancer lesions (squares), a significant inverse linear correlation was found between the average voxel intensities of the MRS-suspicious regions and the Weighted Distances (WD) to the corresponding histological cancer lesions. This indicates higher metabolomic values the closer the corresponding MRS region and histological cancer lesion are located. pT3 tumor lesion shown as circle.<sup>104</sup>

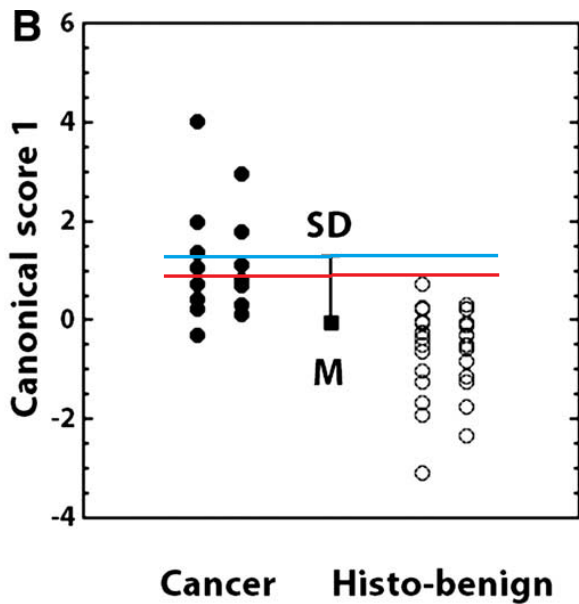


**Figure 22 Possible effect of a lowered threshold.** In the preliminary study, the profile values of all voxels corresponding with a benign histology fell under the empirical threshold of median (M) plus one standard deviation (SD) (marked in blue). With the reduction of the threshold to median plus 0.75 SD (marked in red) as an alternative analysis, a higher detection rate of cancer lesions is expected. However, an elevated number of regions with benign histology might falsely be considered as suspicious as a consequence of the lower threshold.<sup>104</sup>



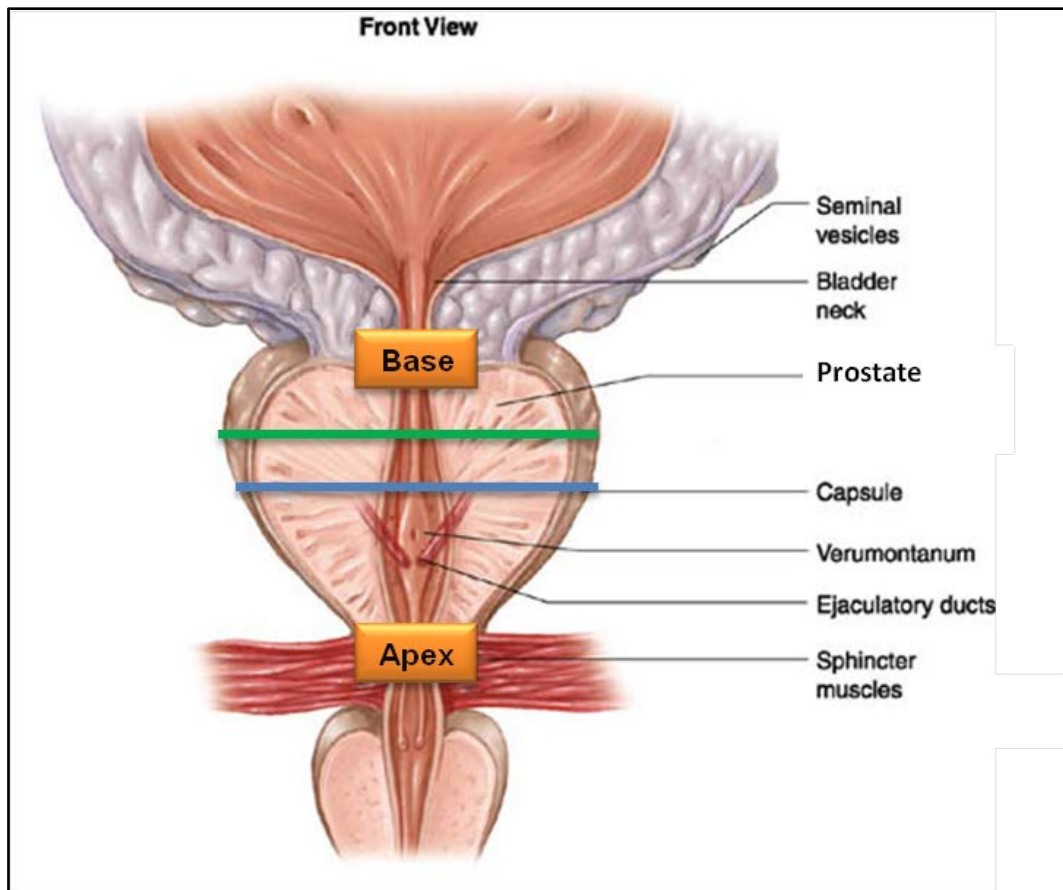


**Figure 23 Prostate anatomy.** The ovally shaped prostate has a broadened base cranial and a smaller apex caudal. The transverse slice with the highest diameter and therefore biggest surface (green line) lies close to the middle cross-sectional plane (blue line) but is shifted towards the prostate base. [image copyright: [www.paradoja7.com](http://www.paradoja7.com)]

## Tables

Name	From [ppm]	To [ppm]	OverallLF
Normalization	0	100	0
4.14-4.1	4,095	4,145	0,205911065
_4.05_	4,045	4,055	-0,011865615
3.99-3.96	3,955	3,995	0,036663702
3.94-3.93	3,925	3,945	0,008994109
_3.78_	3,775	3,785	-0,0638283
_3.75_	3,745	3,755	0,392315522
3.74-3.71	3,705	3,745	0,271976331
_3.63_	3,625	3,635	0,198159819
_3.62_	3,615	3,625	0,020006714
_3.6_	3,595	3,605	-0,113261954
_3.34_	3,335	3,345	0,001499755
_3.29_	3,285	3,295	0,01276959
_3.27_	3,265	3,275	0,007992613
_3.26_	3,255	3,265	0,100962271
_3.24_	3,235	3,245	-0,216015438
_3.22_	3,215	3,225	0,305143666
_3.2_	3,195	3,205	-0,010531546
3.15-3.1	3,095	3,155	-0,13368319
3.09-3.05	3,045	3,095	-0,100085933
_3.03_	3,025	3,035	-0,224970081
_2.71_	2,705	2,715	0,095828226
_2.68_	2,675	2,685	-0,02455364
_2.55_	2,545	2,555	0,007052172
_2.52_	2,515	2,525	0,085057193
2.45-2.43	2,425	2,455	-0,020142958
2.42-2.4	2,395	2,425	0,13530547
_2.36_	2,355	2,365	0,202463704
_2.35_	2,345	2,355	0,317678047
_2.34_	2,335	2,345	-0,089473156
2.33-2.3	2,295	2,335	-0,178150419
_1.47_	1,465	1,475	-0,255390312
_1.33_	1,325	1,335	-0,13247636
_1.28_	1,275	1,285	0,065076259
_1.2_	1,195	1,205	-0,068592123
0.96-0.93	0,925	0,965	0,00311299
_0.9_	0,895	0,905	0,181138016

**Table 4 List of the overall loading factors.** The table shows the overall loading factors for all the 36 metabolite regions that were included into the process of Profile Fitting. Shown are the locations of those regions and the specific loading factors. The more cancer-specific elevations of a metabolite region are, the higher the overall loading factor.

<b>MI cut-off values</b>	<b>Sensitivity</b>	<b>1 - Specificity</b>
5.67	1.000	1.000
7.00	1.000	0.977
7.52	1.000	0.953
8.34	1.000	0.930
9.10	1.000	0.907
9.63	1.000	0.884
10.42	1.000	0.860
11.85	1.000	0.837
13.21	0.962	0.837
13.57	0.962	0.814
13.77	0.962	0.791
13.95	0.962	0.767
14.36	0.962	0.744
14.87	0.923	0.744
15.25	0.923	0.721
15.54	0.885	0.721
16.62	0.846	0.721
18.10	0.846	0.698
19.94	0.846	0.674
21.89	0.846	0.651
22.79	0.846	0.628
23.75	0.808	0.628
25.08	0.808	0.605
26.29	0.808	0.581
27.11	0.808	0.558
28.01	0.808	0.535
29.79	0.808	0.512
31.63	0.808	0.488
32.44	0.808	0.465
33.11	0.769	0.465
33.93	0.731	0.465
35.35	0.692	0.465
36.91	0.692	0.442
38.66	0.692	0.419
40.12	0.692	0.395
41.81	0.692	0.372
43.67	0.692	0.349
44.27	0.692	0.326
<b>45.87</b>	<b>0.692</b>	<b>0.302</b>
47.43	0.654	0.302
47.98	0.654	0.279
49.35	0.615	0.279
51.62	0.577	0.279
52.94	0.577	0.256
53.46	0.538	0.256
53.97	0.538	0.233

54.86	0.500	0.233
56.18	0.462	0.233
56.86	0.462	0.209
58.09	0.423	0.209
60.92	0.423	0.186
63.40	0.423	0.163
70.60	0.385	0.163
80.92	0.346	0.163
89.56	0.346	0.140
95.84	0.308	0.140
98.48	0.269	0.140
103.05	0.269	0.116
107.57	0.231	0.116
110.33	0.192	0.116
112.00	0.192	0.093
115.18	0.192	0.070
119.25	0.192	0.047
121.71	0.154	0.047
125.17	0.115	0.047
145.63	0.077	0.047
165.56	0.077	0.023
169.24	0.077	0.000
180.23	0.038	0.000
189.95	0.000	0,000

**Table 5 Coordinates of the Malignancy Index ROC curve.** The table shows different cut-off values of the MI (with values above indicating malignancy) and the associated sensitivity as well as 1-specificity. The highest values for both parameters are obtained with a MI cut-off value of 45.87. Here, a sensitivity of 69% and a specificity of 70% are achieved. Lower MI cut-off values would result in higher sensitivity levels (however at an expense of a lower specificity), which might be of advantage for screening tests.

## **Acknowledgements**

I am very grateful to Dr. L. L. Cheng (Harvard Medical School, Boston) for his continuous mentorship and the provision of my own research project. I am equally grateful to Prof. Dr. T. Bley (Universitätsklinikum Würzburg) for the enriching guidance within the last years. A special thanks goes to Dr. J. Nowak, who made this research project as well as the Boston stay possible and who became an invaluable contact person for all questions about writing a dissertation.

I furthermore have to thank my fellow medical students A. Maxeiner, F. Sturm, J. Hein, P. Knape and M. Köhler, who performed the MR scanning of the 30 prostate samples. I also have to thank E.-M. Ratai for the technical support during the scanning as well as for all her patience in explaining MRSI details to me, S. Wu for the detailed histopathological evaluation and the training in the Gleason grading scheme and E. Decelle for her motivation, continuous support and excellent help on language issues.

I am very grateful to Y. Berker, who developed the software for the (partial) automation of the spectral analysis. I also want to thank Dr. J. Hain for all his advices regarding data analysis and statistics.

Finally, I would like to express my high gratitude to my family, boyfriend and friends for their support, motivation and patience.

## **Statement of Authorship**

Hiermit erkläre ich, Romy Langhammer, geboren am 18.11.1990 in Eisenach, an Eides statt, dass die vorgelegte Arbeit von mir selbst und ohne die unzulässige Hilfe Dritter verfasst wurde, auch in Teilen keine Kopie anderer Arbeiten darstellt und die benutzten Hilfsmittel sowie die verwendete Literatur vollständig angegeben sind.

---

Ort, Datum

---

Unterschrift

## **Curriculum Vitae**

Auf eine Veröffentlichung des Lebenslaufs wurde in der elektronischen Version aus datenschutzrechtlichen Gründen verzichtet.